USE OF OPTICAL METHODS FOR STUDYING PHOTOCURRENT GENERATION MECHANISM IN SILVER NANOWIRES AND DEFECTS IN GLASS

A THESIS SUBMITTED TO

THE GRADUATE SCHOOL OF ENGINEERING AND SCIENCE

OF BILKENT UNIVERSITY

IN PARTIAL FULFILLMENT OF THE REQUIREMENTS FOR

THE DEGREE OF

MASTER OF SCIENCE

IN

MATERIALS SCIENCE AND NANOTECHNOLOGY

By

Merve Üstünçelik

June 2021

USE OF OPTICAL METHODS FOR STUDYING PHOTOCURRENT GENERATION MECHANISM IN SILVER NANOWIRES AND DEFECTS IN GLASS

By Merve Üstünçelik

June 2021

We certify that we have read this thesis and that in our opinion it is fully adequate, in scope and in quality, as a thesis for the degree of Master of Science.

Talip Serkan Kasırga(Advisor)

Bülend Ortaç

Hüsnü Emrah Ünalan

Approved for the Graduate School of Engineering and Science:

Ezhan Karaşan
Director of the Graduate School

ABSTRACT

USE OF OPTICAL METHODS FOR STUDYING PHOTOCURRENT GENERATION MECHANISM IN SILVER NANOWIRES AND DEFECTS IN GLASS

Merve Üstünçelik
M.S. in Materials Science and Nanotechnology
Advisor: Talip Serkan Kasırga
June 2021

The light-matter interaction covers a wide range of physical phenomena which can be used for the investigation of materials. This interaction can be used both spectroscopically and microscopically to investigate fundamental material properties such as structural, optical, and electrical properties. In this thesis, I used optical methods to characterize materials on macro and nanoscales based on different light phenomena such as scattering, transmission, absorption, and reflection. First, I used Raman spectroscopy in a diffraction-limited setup to show that the trapped gas inside the bubble defects can be identified in a matter of seconds non-destructively. Also, I investigated near-field methods to gain further understanding about chemical, optical and structural information in nanomaterials by using an aperture-based transmission mode Near-field Scanning Optical Microscopy (SNOM). Finally, I used scanning photocurrent microscopy to demonstrate photocurrent generation in silver nanowires and nanowire networks. This thesis demonstrates that light-matter interaction can provide useful information in the characterization of a vast class of materials. The advantages of the non-destructive Raman technique in defects analyses, the challenges of working in the near-field region in nanomaterials characterization, and also the photocurrent generation in silver nanowires for the first time have been demonstrated with experimental results.

Keywords: Raman Spectrocopy, Aperture-SNOM, Near-field Raman, 2D materials, Scanning Photocurrent Microscopy, Near-field Scanning Photocurrent Microscopy, Glass defects, Silver Nanowire.

ÖZET

GÜMÜŞ NANOTELLERDE FOTOAKIM ÜRETİM MEKANİZMASINI VE CAMDAKİ KUSURLARI İNCELEMEK İÇİN OPTİK YÖNTEMLERİN KULLANIMI

Merve Üstünçelik
Malzeme Bilimi ve Nanoteknoloji , Yüksek Lisans
Tez Danışmanı: Talip Serkan Kasırga
June 2021

Işık-madde etkileşimi, malzemelerin araştırılması için kullanılabilecek çok çeşitli fiziksel olayları kapsar. Bu etkileşim, yapısal, optik ve elektriksel özellikler gibi temel malzeme özelliklerini araştırmak için hem spektroskopik hem de mikroskobik olarak kullanılabilir. Bu tezde, saçılma, iletim, absorpsiyon ve yansıma gibi farklı ışık fenomenlerine dayalı olarak makro ve nano ölçekte malzemeleri karakterize etmek için optik yöntemler kullandım. İlk olarak, kabarcık kusurlarının içinde hapsolmuş gazın birkaç saniye içinde tahribatsız bir şekilde tanımlanabileceğini göstermek için kırınım sınırlı bir kurulumda Raman spektroskopisini kullandım. Ayrıca, bir açıklık tabanlı iletim modu Yakın Alan Taramalı Optik Mikroskobu (SNOM) kullanarak nanomalzemelerdeki kimyasal, optik ve yapısal bilgiler hakkında daha fazla bilgi edinmek için yakın alan yöntemlerini araştırdım. Son olarak, gümüş nanotellerde ve nanotel ağlarında fotoakım oluşumunu göstermek için taramalı fotoakım mikroskobu kullandım. Bu tez, ışık-madde etkileşiminin, geniş bir malzeme sınıfının karakterizasyonunda yararlı bilgiler sağlayabileceğini göstermektedir. Tahribatsız Raman tekniğinin kusur analizlerindeki avantajları, nanomalzemelerin karakterizasyonunda yakın alan bölgesinde çalışmanın zorlukları ve ayrıca gümüş nanotellerde ilk kez foto akım üretimi deneysel sonuçlarla gösterildi.

Anahtar sözcükler: Raman spektroskopisi, açıklı-SNOM, Yakın-alan Raman, 2B malzemeler, Taramalı Fotoakım Mikroskobu, Yakın-alan Taramalı Fotoakım Mikroskobu, Cam Kusurları, Gümüş Nanotel.

Acknowledgement

First of all, I am very grateful to Almighty Allah Who has given me the courage and the determination to be able to pursue my curiosity and then to accomplish my dream. In addition, I would like to express my deep appreciation to my ancestors and martyrs who have sacrificed their lives for our freedom. I want to thank the following people who posses huge importance in the completion of this thesis. I would like to express my gratitude to my advisor Dr. Talip Serkan Kasırga for his academic mentorship and also the opportunities which he has given me throughout my Master's degree to work in such a fascinating field under his guidance. I owe a sense of gratitude to Dr. Bülenç Ortaç for his valuable comments along with the technical support, Dr. Alpan Bek for his kind suggestions on my work and Dr. H.Emrah Ünalan for the collobration of nanowire study. It is hard to imagine finishing this journey without the support and endless care of my family. I would like to thank my father Mehmet Üstünçelik, my mother Emine Üstünçelik, and my brother Mustafa Üstünçelik, from the core of my heart. Moreover, I would like to express my warm appreciation to my close friends Feride Çeçen and Muhammad Junaid Iqbal who have always supported and motivated me in tough times. I also would like to acknowledge SCM Lab members for their help in the lab work, especially to my labmate M.Ali Razeghi for his contribution to the silver nanowire study. I would like to acknowledge all my friends for the good times we have shared during the period of the master's study.Lastly, I would thank profusely to UNAM operation team Mustafa Güler, Semih Bozkurt, Övünç Karakurt, and Murat Güre for their kind help and patience during the field of work.

Contents

List of Figures

Chapter 1

Light-matter interaction

The nature of light and matter itself, light interaction with matter were main questions that are worthy to study throughout the history of science. The term *light-matter interaction* comprises a wide range of physical phenomena from classical physics to quantum electrodynamics or from black holes to nanophotonics.The term *interaction* is used to imply that light and matter are different entities that may affect one another via some intermediary[1].In this study, the different actions of matter and light (see figure 1.1) are concerned as listed following articles.

- Transmission
- Scattering
- Reflection
- Absorption

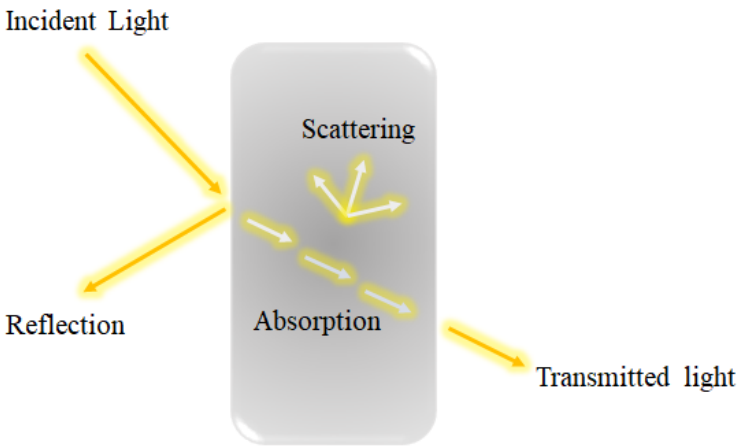

Figure 1.1: Geometry of light-matter interaction

Having interaction with a smooth surface, the incident light bounces back by surface land upon which is called the reflection of light. The reflecting surface is considered as a physical boundary between different refraction indices matters [2].In 1672, Isaac Newton's prism experiment remind the importance of reflection of light and caught attentions on the light-matter interaction. He did not only explore the nature of light, also observed the presence of evanescent waves via the famous prism experiment even though he was not able to realise at that time. In the experiment, the incident light was tried to send through the two identical prisms. While the lights mostly reflected from the first prism, only way to observe the passage of the light through these two identical prisms was possible within a few tens of nanometers. At that time, he was not able to explain the existence of near-field but this experiment has become a model to understand the propagation of evanescent wave. Since the non-propagating evanescent waves stays at the interface of the first prism, the collected non-propagating evanescent waves can be transformed to the propagating evanescent wave by placing the second prism a few tens of nanometers vicinity of the surface. Based on Newton's experiment, the propagation behavior of the near-field evanescent waves can be seen in the figure 1.2.

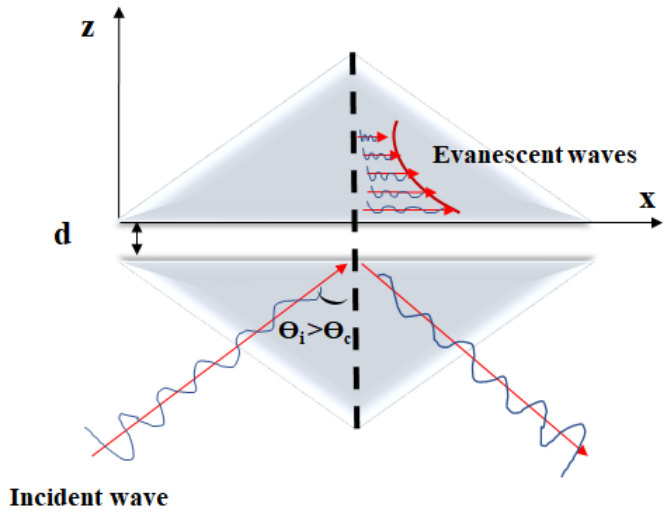

Figure 1.2: Excitation of an evanescent wave by total internal reflection

Many years later of his observation, the existence of near-field region brought another dimension to light- matter interaction ,especially for the materials in nano size ranges.It was formulated by Abbe that the major limitation of optical microscopy for the resolution was due to the nature of the light. Because the high spatial frequency components of the light can not be able to be reached by resolution limited microscopy. Almost after half a century, Irish scientist Synge proposed an idea to overcome the diffraction and resolution limit of optical microscopy. According to his proposal, the diffraction limit could have been broken by bringing a subwavelength aperture into the close vicinity of the sample surface called the near-field zone, to be able to collect the high-spatial frequency information of the sample. Thus it would have been possible to collect evanescent field components with the far-field detector[3]. Diffraction-limit was overcome by near-field microscopy methods so the optical, structural, electronic, and chemical properties of the matter at the local level was able to obtained. As it shown in this study, the transmission of the light can carry these importance information of matter from near-field region to far-field detector. The details of the *transmission-mode Scanning Near-field Optical Microscopy* experiment can be found in Appendix.

In the process of light scattering, electromagnetic radiations deviate from a straight pathway. When light interacts with matter that has microscopic surface irregularities, the light will diffuse instead of reflecting. This light scattering phenomenon can provide the fingerprint information of matters as in Raman spectroscopy measurement[4].As depending on the incident photon energy and the conversion of its energy, scattering takes place either elastically or inelastically. An elastically scattering process which is called Rayleigh carries the same frequency and energy as the incident photon. There is a special relationship between scattered light intensity and the diffraction index, so the Rayleigh scattering becomes inversely proportional to the fourth power of wavelength of light ($I_s \sim \frac{1}{\lambda^4}$).The behavior of Rayleigh scattering within the visible spectrum is illustrated as comparing with the Infrared and Ultraviolet region in figure 1.3[1].

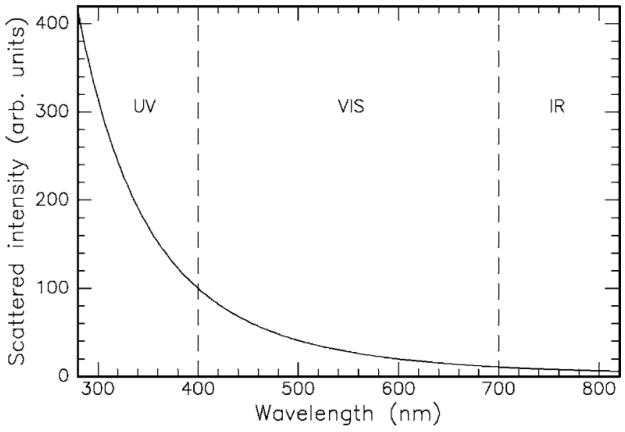

Figure 1.3: Rayleigh's law of scattering. Image extracted from [1]

On the other hand, the inelastically scattered photon energy is different than the incident photon energy and known as the Raman effect. The discovery of *the Raman effect.* emerged as a result of the long discussions between great scientists for the real reason behind the blue color of the Mediterranean Sea. By 1871s, Lord Rayleigh had analyzed the scattered sunlight and he concluded the intensity of the scattered light was inversely proportional to the fourth power of the wavelength[19]. According to Rayleigh's observation, the color of the Mediterranean Sea was not just more than the reflection of the blue sky[20]. The Indian scientist Chandrasekhara Venkata Raman was unsatisfied with Rayleigh's explanation for the reason for the color of the sea. Raman decided to focus on the light scattering phenomenon and further detailed his observation by the experiment he performed with simple equipment he had. In March 1928, the audience was stunned in the lecture after hearing the discovery of the Indian physicist. He simply explained his observations as "*a new kind of radiation or light emission from atoms and molecules*" [21]. The experimental setup of the Raman is demonstrated in figure 1.4.

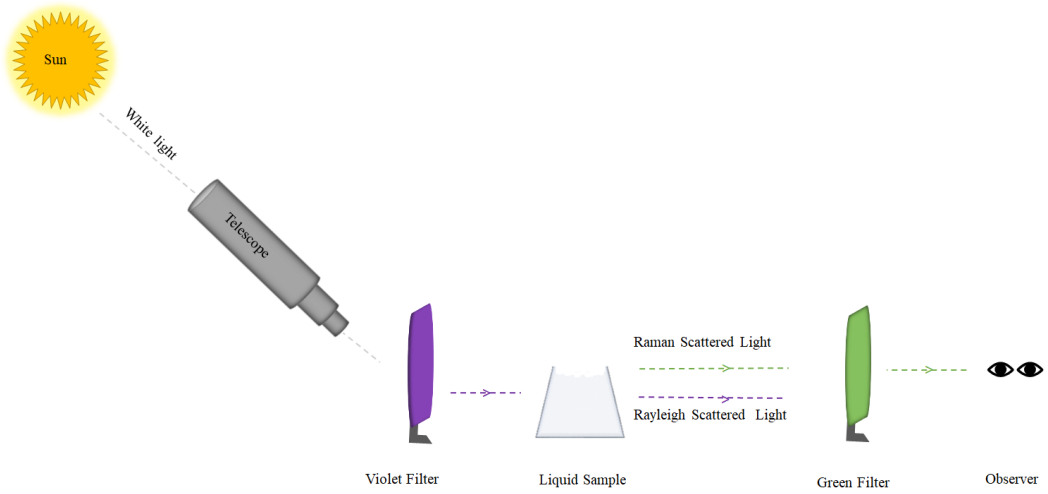

Figure 1.4: Schematic demonstration of the discovery of the Raman effect

Raman took advantage of the sunlight as high intensity light source. The white light source collected by the telescope and sent through the violet filter; a monochromatic filter. Filtered lights were underwent scattering while passing through the liquid sample. Most of the passing lights were the same color with incident violet light. These were later called Rayleigh scattered light. However, Raman observed that some scattered lights were in different colors than Rayleigh's scattered lights. Therefore, he placed another filter (green) behind the sample and could isolate the green light. After observing the same effect on series of liquid samples, the inelastic scattering was reported as secondary radiation in Nature by Raman. The reporting of this effect took time because of the inadequate intensity light source. A high-intensity light source was needed in the experiment to be able to observe the weak Raman effect. At that time sunlight was the available light source which can be converted to a highly intense light source by using the refracting telescope[21]. However, the basic components of the instrument were replaced by the improved instrumentation by time. Various kind of components were tried in place for light and the detection system, until reaching the commercial development state of art present Raman spectroscopy. Helium, Zinc, Lead and Bismuth were the first light sources to be embedded the system, however, their low light intensities were not high enough to proceed the studies. By the invention of laser around 1960s, the weak lamp lights were replaced with the high intensity laser sources such as NdYAG, Kr^+ and Ar^+. The lasers became the mostly preferred radiation source today in Raman spectroscopy. A laser beam can be demonstrated as propagation of the plane electromagnetic wave as in figure 1.5.

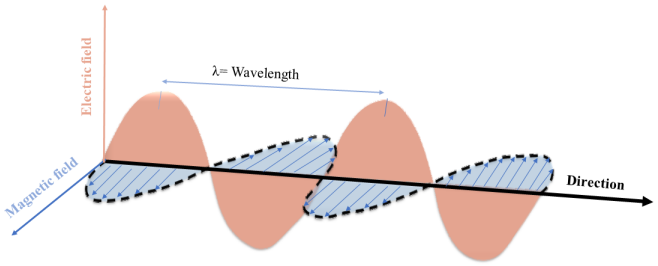

Figure 1.5: Demonstration of linear polarized electromagnetic wave

The electric and the magnetic components of the polarized electromagnetic waves travel in the z-axis perpendicular to each other[22].The electromagnetic radiations are classified according to their wavelength (λ). It is beneficial to understand the relationship of energy ($\Delta\varepsilon$) with other scales such as frequency (ν), speed of light (c), wavenumber (ω) , because the interaction of electromagnetic radiation with molecular states is examined in Raman spectroscopy. The equations (1.1), (1.2) and (1.3) shows the relationship between the scales [23].

$$\lambda = \frac{c}{\upsilon} \tag{1.1}$$

$$\nu = \frac{\Delta\varepsilon}{h} \tag{1.2}$$

where h is a constant called Planck's constant

$$\omega = \frac{\nu}{c} = \frac{1}{\lambda} \tag{1.3}$$

According to the equations, it can be understood easily that the highest energy radiations will have the lowest wavelength and vice versa. When electromagnetic radiation like a single-frequency laser beam interacts with the molecules of the matter, it causes the polarization of the cloud of electrons around the nucleus. Thus, a short-lived state called a virtual-state is created and the different vibrational unit of energy is detected by Raman. This created virtual state is not stable and re-radiation of photons can take place quickly.When a photon absorption or excitation of an electron to the higher place takes place, the energy of a molecule gains a number of different degrees of freedom. There are three degrees of freedom present for the translation of the molecule in space and the other three degrees stand for the rotational movement which is the movement way of linear molecules. For instance, the number of the vibrational degrees of freedom can be calculated in such a way that if the N represents the number of atoms in a molecule, 3N-5, and 3N-6 is considered as a linear and non-linear molecule respectively. According to this, only one vibration movement takes place in a diatomic molecule. Although this movement can change the polarizability of the molecule, there will be no change in dipole since the vibration takes place around the mass center of the molecule symmetrically. Therefore, the change in polarizability will give a band in the Raman spectrum while detecting the oxygen gas but no infrared spectrum. It is now can be understood that to be able to detect the Raman spectrum of the matter, their vibrational modes have to be *Raman active*. The three atomic molecules like H_2O and CO_2 will have three vibrational modes as symmetrical stretch, asymmetric strength, and bending or deformation. These modes are demonstrated by *the spring and ball model* as in figure 1.6 [23] [24].

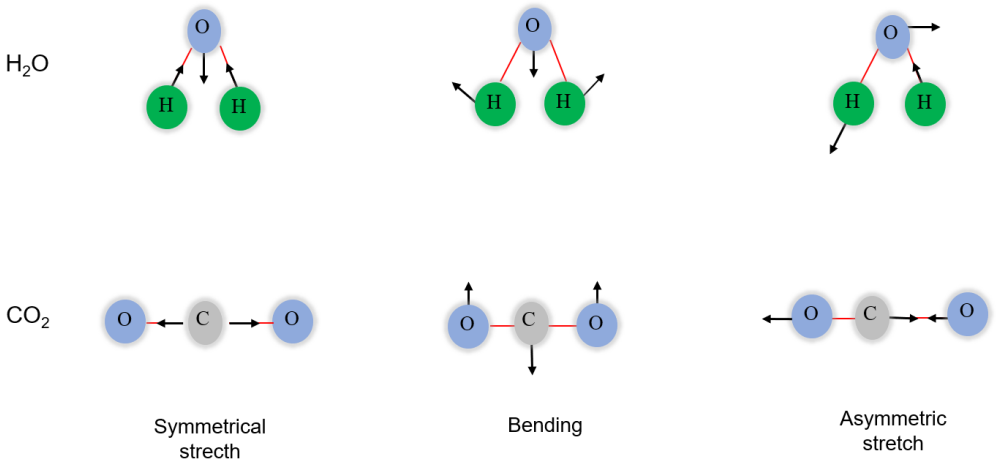

Figure 1.6: The spring and ball model

In the model, while spring stands for the bonds between atoms, a ball is used to demonstrate the atoms. So, the vibrational frequency is related to the mass of atoms and the bond strength. Therefore, the lower vibrational frequency is obtained in the combination of heavy atoms and weak bonds. On the other hand, the higher vibration frequency results from the combination of the strong bond and the light atoms. In the following figure 1.7, the changes in the polarization of the CO_2 molecule structure are demonstrated by the electron cloud cover the three-dimensional structure in different patterns. Once the molecule is vibrated by external stimuli, the electron cloud around the whole molecule will change the charge polarization. Thus, the dipole moment or the polarization of the molecule changes. In the example of CO_2, the symmetrical stretch vibration mode causes a large amount of polarization change and as a result of this, the strong Raman scattering and no dipole change take place. Therefore, the extended and compressed deformation of the molecule can be observed in Raman spectroscopy, not in Infrared spectroscopy[23].

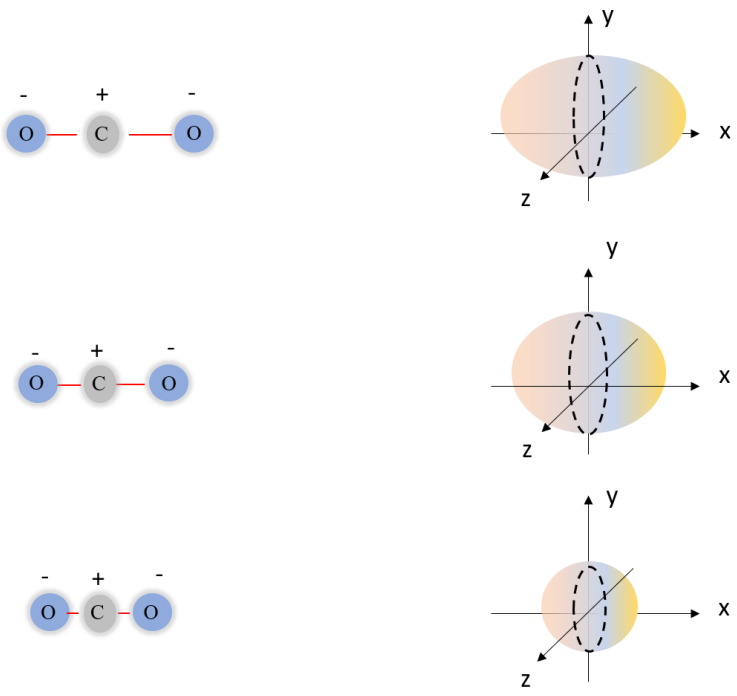

Figure 1.7: The symmetric stretching of the CO_2 molecule

To sum up, the scattered light is the combination of Rayleigh and Raman Scattering. While Rayleigh scattering has the same frequency with the incident beam (ν_0),The Raman scattering is weaker than the incident beam ($\backslash 10^{-5}$ of incident beam) and has $\nu_0 \pm \nu_m$ frequency, which υ_m is the abbreviation of the vibrational frequency of a molecule. In Raman Spectroscopy, the vibrational frequency is measured as a shift from the incident beam frequency. Therefore, there are two important lines are emerged into Raman system. The one which is $\nu_0 - \nu_m$ called as the Stokes line, and $\nu_0 + \nu_m$ is another line which is called anti-stokes. Raman spectra are taken in the region where both Raman lines and the excitations are observable which is the UV-region. Theoretically, The Raman Scattering can be expressed by equations where E is the oscillating electric field of the photon, E_0 is the amplitude at a given time (t) and with the frequency of monochromatic source (ν) [22].

$$E = E_0 \cos 2\pi\nu_0 t \tag{1.4}$$

When a matter is irritated by the monochromatic light source, an electrical dipole moment (P) is created as a result of the excitation and conversion of the molecules.

$$P = \alpha E = \alpha E_0 \cos 2\pi\nu_0 t \tag{1.5}$$

The polarizability of the molecule α can be expressed as follows:

$$\alpha = \alpha_0 + \alpha' \cos 2\pi\nu_m t \tag{1.6}$$

While α_0 represents the polarizability of a molecule at equilibrium condition, $a^{'}$ demonstrates the change in polarizability with molecular vibration. ν_m is used for the vibrational frequency of a molecule. Since the different molecular deformation has different characteristic vibrational frequency (ν_m) the amplitude of the vibrational modes q_0 is linked with the nuclear displacement q_0 as follows:

$$q = q_0 \cos 2\pi\nu_m t \tag{1.7}$$

When combining the equations (1.5)and (1.6), this relationship is obtained.

$$P = [\alpha_0 + \alpha' \; cos 2\pi\nu_m t].E_0 cos 2\pi\nu_0 t \tag{1.8}$$

Equation (1.8) can be divided into three parts are the important characteristic frequencies of the emitted photons from the oscillating dipole can be seen in this way:

$$P = \alpha_0.E_0 \cos 2\pi\nu_0 t + 0.5a'.E_0[\cos 2\pi(\nu_0 + \nu_m)t + \cos 2\pi(\nu_0 - \nu_m)t] \qquad (1.9)$$

The first term (ν_0) represents the Rayleigh scattering which has the same frequency as the incident beam and also it does not carry any spectroscopic information. The last two terms are Raman scattering frequencies of (ν_0+ν_m) and (ν_0-ν_m) are called as anti-Stokes and Stokes. The energy diagram of these three types of radiation is illustrated in the figure 1.8. As it can be understood from the energy level diagram that there has to be some change in molecular vibration frequency, otherwise no Raman scattering will be able to observe as a result of not lead to a no change in polarizability. Depending on the wavelength of the irradiation source, the molecular vibration or rotational modes display a characteristic frequency shift on the Raman spectrum. The spectral collection of these characteristic frequencies is considered as unique fingerprint information of each molecule. Therefore, Raman shifts make it possible to both identify the material and analyze its structure [22].

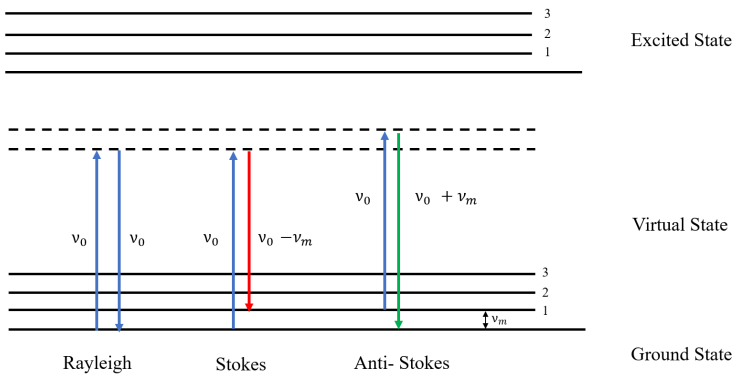

Figure 1.8: Energy level diagram for Raman scattering

The final light-matter interaction phenomenon wherein the scope is of this study is absorption.When a incident light beam is impinged to surface of a matter, some portion of light is absorbed via the matter instead of reflecting back from surface.According to the Bouguer-Lambert law, the absorbed light fraction is related to the thickness of the matter and also the way photons interact with the surface of the matter. This relationship can be seen in the equation 1.10 [5].

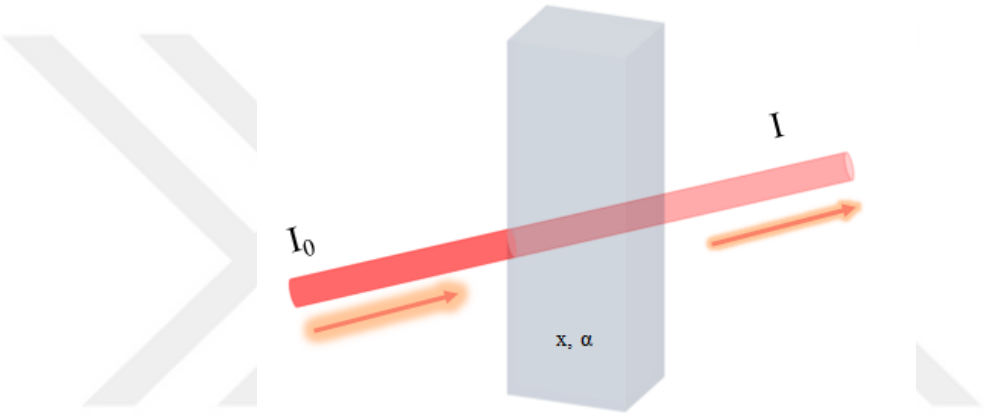

Figure 1.9: Absorption of light according to the Bouguer-Lambert law

$$I = I_0 \exp(-\alpha.x) \tag{1.10}$$

Where I_0,I,α,x represent intensity of the incident beam, intensity of the beam passing the material, characteristic linear absorption coefficent of a material and the path which photons move respectively.

The Rayleigh and Compton scattering are two mechanism that take place in absorption process. The scattering of a photon after an interaction with electron result with loosing some of enegry of the photon which is called the compton scattering.[5]Like in Compton scattering, photoelectric effect is also mechanism which results with energy loss after photon matter interaction. In the photo-electric absorption process, the energy of a photon is consumed to be ejected an electron from the nucleus of atom. It is an important effect since the photocurrent may occur as a result of the photoelectric effect [6].

Photocurrent generation gains importance in photodetectors which are quite beneficial devices used in daily life from imaging to optical communications and storing information. In addition to other photocurrents mechanisms which are driven by the electric-field separation of electron-hole pair, there are also mechanisms such as photo-thermoelectric and photo-bolometric effects which are responsible for the modulation or generation of the photoresponse in optoelectronic devices [11]. In the scope of this study, *the photo-bolometric effect* will be addressed as a photocurrent generation mechanism of devices.The bolometer was invented in 1878 by American astronomer Samuel Pierpont Langley[58].Bolometers are widely used devices in the field of astronomy and particle physics because they can transduce and the absorbed radiation into an increase in temperature where creates variations in resistance of the materials, that can be obtained as electrical signals to read the information [59]. The development of nanomaterials has been provided a new platform for bolometers which having more flexibility, sensitivity, and speed in measurements. For example, the macroscale assemblies of semiconducting single-wall carbon nanotubes showed the bolometric effect due to the effective transfer of the absorption of energy on crystal lattice through strong electron-phonon interaction which results in an increase in temperature[60].In 2D materials photodetector, the photocurrent mechanism based on the bolometric effect can be explained as the change in resistivity of the material stems from the heating via photon absorption.

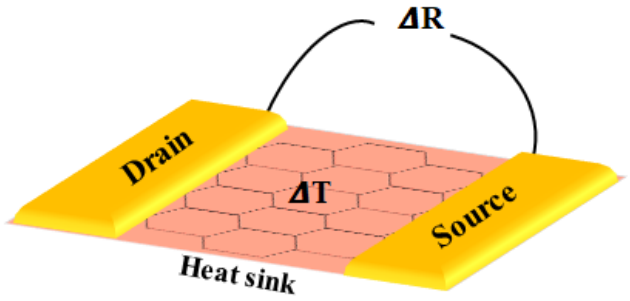

Figure 1.10: Demonstration of photo-bolometric effect photocurrent generation mechanism

The conductance variation of the material with temperature increase and laser heating induced homogeneous temperature increasing significantly play roles in the magnitude of this effect[11]. Once temperature affects the resistivity of the material, the current fluctuation is observed at a applied fixed bias voltage. An external bias is required to produce the photocurrent which means that currents do not self-drive in the system because the magnitude of the current flow can only be modified under external illumination and applied bias.Here the equation 1.11 shows the change in the voltage [61]:

$$\Delta V = I_{DC} \Delta R = I_{DC} \frac{dR}{dT} \tag{1.11}$$

where I_{DC} is the applied DC bias voltage.

In the photo-bolometric effect, the increase in photocurrent is observed with the applied external bias. On the other hand, the sign of the photocurrent strongly depends on the fluctuations on increase or decrease of resistivity and temperature in the system[61].The photo-bolometric effect has been shown on the hot electron bolometer by using dual gated bilayer graphene [62] and also thermalconductivity measurements performed on nanosheets based on bolometric effect[63].

Chapter 2

Methods

2.1 Scanning Photocurrent Microscopy

One of the members of the scanning probe microscopy family is the scanning photocurrent microscopy (SPCM). Instead of using a metal probe like in the operation of AFM or STM, a focused light beam is used in SPCM as a local excitation source.Once a semiconductor locally exited into a non-equilibrium state, the injected electrons and holes are gone through some relaxation process which includes recombination, drift, and thermal relaxation in the semiconductor. At this point, the photocurrent generation is observed if the injected electron or holes reach the electrodes nearby before recombination. The photocurrent as a function of excitation location can be mapped and as a result of this, quite useful information about the optoelectronic properties of semiconductors can be obtained [7].For instance, SPCM has been used in the characterization of semiconductor nanowires[8], graphene[9], and layered transition metal dichalcogenides[10][11]. Since the conventional scanning probe techniques do not fulfill the requirements for working within the sub-wavelength region, the local characterization of the devices is necessary to have a better understanding of the role of the structural properties of the materials on the device's performance. Therefore, *the Scanning Near-Field Photocurrent Microscopy (NSPM)* is a powerful technique

that can provide a high spatial resolution and overcome the drawbacks of the diffraction-limited scanning probe techniques. Besides, having the advantage of non-destructiveness of technique, working within the near-field region makes it possible to reach local properties of the materials like electrical transport at the nanoscale[12].The wide range of applicability of aperture-based near-field scanning photocurrent microscopy has been shown on the charge transfer and the photocurrent generation at single and multilayer graphene interfaces with around 50nm resolution[13].Also,in estimating the dopant concentration of the Si p-n junction under the reverse bias condition [14],understanding the relation between photoresponse and morphology on the defects[15]and in the observation of the local photocurrent on inhomogeneities of solar cells[16][17]. The details of the near-field scanning photocurrent measurements can find in the Appendix section.

2.1.1 Experimental set up

The components of the SPCM setup used in the experiments can be seen in the figure 2.1. A diffraction-limited 532nm laser beam is chopped mechanically around 2kHZ in order to modulate the frequency of the light source, thus decreasing the electrical noise of the photocurrent signal. The modulated frequency is then fed into the lock-in amplifier to use as a reference signal. The lock-in amplifier can extract the genuine signal from the noise with high sensitivity and also remove the contribution of the dc component signal and amplifies the signal that is resulting from the referenced laser beam. There is a photodetector whose output is detected with a second lock-in amplifier, embedded to set up to be able to measure the reflected light from the sample as a function of laser position. The laser beam is focused on the surface of the sample with a 40X objective by passing through optics like the 50:50 beam splitter and the filter. Two probes are served to measure the photocurrent of the sample. While the voltage bias is applied through one probe connected to a current pre-amplifier, another one is grounded. The output of the current pre-amplifier is fed into the lock-in amplifiers. The measured signal from the photodiode and the current are

simultaneously recorded at each step of the scan. At this point, it is very important to do perform scanning at a slower rate than the integration time of the lock-in amplifiers to limit the noise level.The scan motion in direction of X and Y, the scan and step size,the experimental parameters during scanning and the recordings of real-time observations, the data acquisition, are controlled through the Labview program.Thus, the reflection map of the sample matches with the photocurrent map of the sample, and the location of the photocurrent generation on the sample can be specified easily by monitoring the scan result.[18].

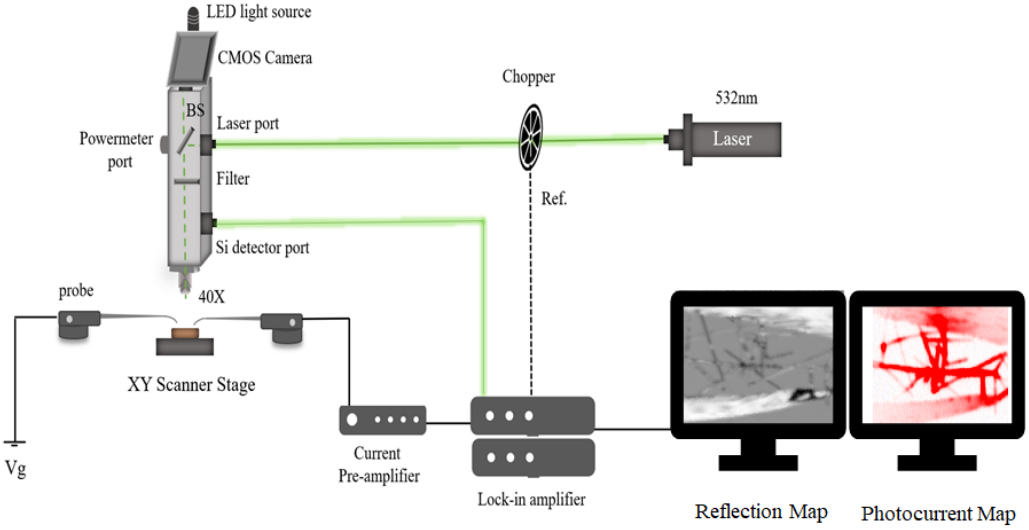

Figure 2.1: Scanning Photocurrent Microscopy Setup

2.2 Raman Spectroscopy

2.2.1 Instrumentation

The Raman system has to be designed in such a way that while the collection of many Raman Scattered photons are possible and the Rayleigh scattering can be eliminated. Therefore, in addition to the main components, the Raman system is equipped with some filters, different types of monochromators, and pinholes to eliminate the contributions of the elastically scattered light which is useless to the system in terms of vibrational information[25].The main components of a Raman system can be listed as follows [22]:

1. Excitation Source
2. Illumination and Optics collection system
3. Wavelength selector
4. Detector

The components of the system used in this study can be seen in the figure 2.2.

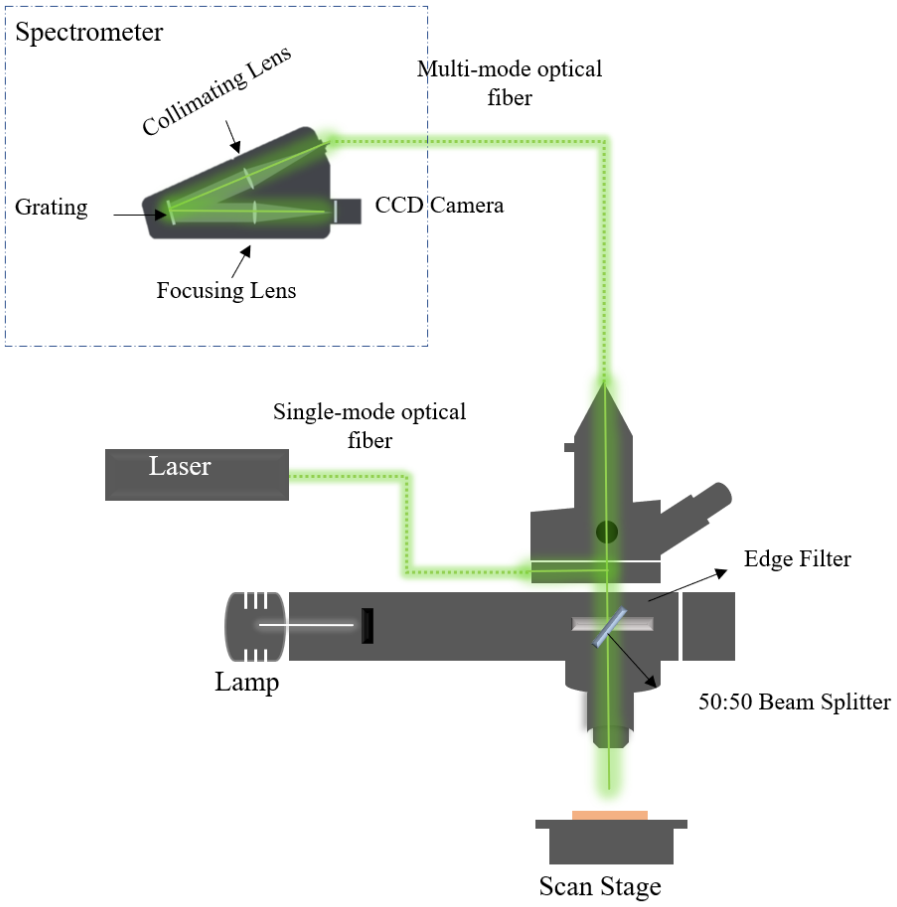

Figure 2.2: Diffraction limited Raman Spectroscopy

1. Excitation Source

   There are many light sources that can be used in Raman spectroscopy especially, continuous-wave lasers (an abbreviation of Light Amplification by Stimulated Emission of Radiations) from Ultraviolet (UV) to the near-infrared (NIR) regions which are demonstrated in the figure 2.3. The intensity of the Raman scattering is proportional to excitation wavelength as the order of λ^{-4},thus the short wavelengths are the source of higher Raman spectral intensity, however, they can also lead to excitation of fluorescence which is observable in the Raman bands[25]. For this reason, the choice of Raman light source is very important. The following five characteristics of the laser beam are the reasons behind integrating the lasers into the Raman system. The first of all, the laser light is a *monochromatic source* which means that the lights waves have same direction and phase, therefore monochromatic laser light can to do focus to a very narrow band of frequencies.Second, the laser light can be concentrated as a high intense small beam (the diameter of the beam can be lowered up to 0.1mm by using simple lens systems) since it is *highly collimated*.The third, the laser lights are ideal for depolarization measurements since they are *linearly polarized*. The fourth reason is coming from the ease of production the laser beams in different wavelength range by using dye lasers or any other devices.The finally, it is possible to work with different *light source powers*,while the large CW laser can provide 1-2W of power easily, pulsed lasers can produce peak powers on the order of 10 to 100MW [22].

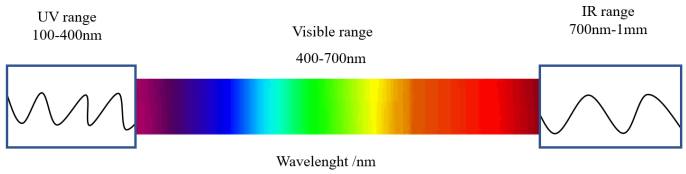

Figure 2.3: Optical wavelength range

2. Illumination and Optics collection system

The optical components of the Raman are necessary for laser alignment and proper measurement. Due to the weakness of the Raman Scattering, the collection of the scattered radiations has to be efficient enough to obtain a meaningful spectrum. Hence, optics are placed in such configurations as 90 and 180 degrees to be able to accomplish the collection of the signals[22].The Raman provides a lateral resolution that mostly depends on the wavelength of the light source and the numerical aperture of the objectives which is integrated into the system. An example objective can be seen in the figure 2.4, the half-angle (α) of the laser cone is defined the numerical aperture of the objective which shows the resolving power of an objective.

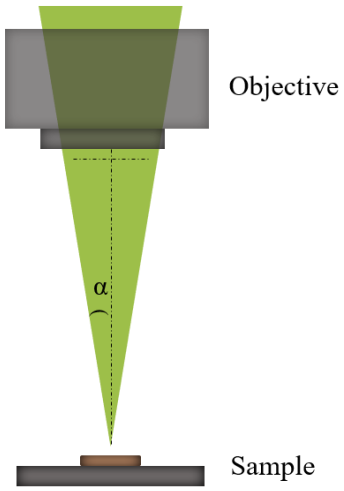

Figure 2.4: The half-angle of the laser cone

The resolution of a classical microscope is expressed by Rayleigh criteria as in equation (2.1) and the obtained image of the two-points object can be seen as in the figure 2.5, according to Rayleigh resolution criteria.

$$\Delta \text{ x} = \frac{0.61\lambda}{NA} \tag{2.1}$$

where

$$NA = n \sin \alpha$$

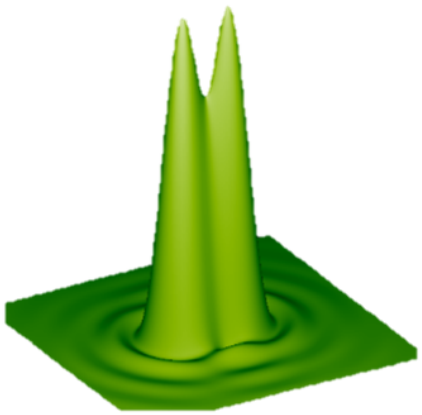

Figure 2.5: Rayleigh criterion

$\Delta\ x$ is the smallest distance between two -point objects, λ is the wavelength of the light source and NA numerical aperture of the objective; n is the refractive index of the medium between the sample and the objective, α stands for the aperture angle of the objective. Since the high lateral resolution is required in the Raman measurements, it is preferred to work with objectives that have a high numerical aperture, hence the objectives are designed by considering the high refractive index mediums such as water, oil, or glycerin.By the combination of short wavelength light source and the high numerical aperture objective, the spatial resolution can be reached up to 200nm[24][26].

3. Wavelength Selector

When the laser is introduced to the system, the filters or spectrometer are responsible for the selection of the wavelength. The special filters are designed to allow the passage of the only desired laser line or remove the other lines, which have to be integrated into the system[25].The spectrometer is the place where the scattered lights are collected and the elimination of the signals is crucial to obtain the correct spectrum. In this step, one of the major challenges of the Raman Spectroscopy arises because the weak intensity Raman scattering takes place at a frequency which very close to the frequency of the irradiation source. Therefore, the weak Raman scattering has to be eliminated from the both laser line and the Rayleigh scattering radiation. By cutting off the spectral range of the laser with laser-blocking filters is the solution to this problem. For this purpose, there are special filters called *edge* and *notch filters* that are worked to "block off" the specific wavelengths.These filters are placed on the laser path before reaching the spectrometer. The transmittance behavior of the filters with respect to laser line is demonstrated in the figure 2.6.

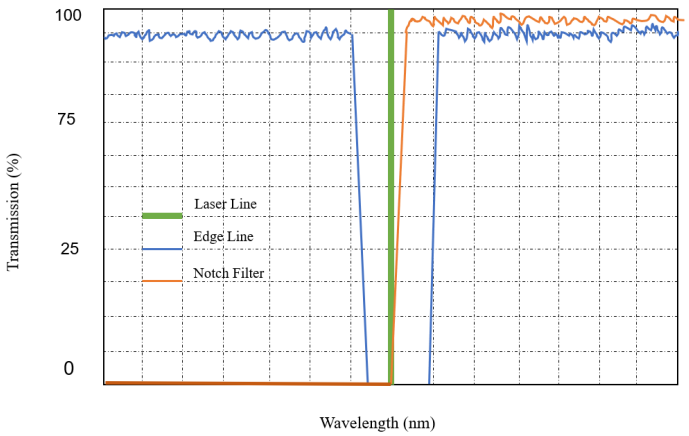

Figure 2.6: Transmittance versus wavelenght

The reason behind the most common usage of the notch filter is because both anti-stokes and stokes scattering can be absorbed. Most of the scattered lights within approximately $200cm^{-1}$ excitation frequency is collected by the notch filter and below or above this range gives the maximum transmittance. On the other hand, the edge filters have two different types: *the shortpass* and*the longpass.* While the long pass filters can block off the wavelengths below the irradiation source, the short pass filters block off all wavelengths above therefore, the long pass filters are suitable to measure Stokes-Raman Scattering and the short pass filters are suitable for Anti-Stokes Raman scattering. The recent updates in technology made edge filters more preferable than the notch filters by offering a high transmittance along with the close cutting edge value to the frequency of the laser. As a result of this improvement, it became possible to detection of the Raman bands even at very short wavenumbers close to the laser line. To sum up, when the sample is irritated with the laser, scattered lights are filtered and the passing lights are dispersed by a diffraction grating so that the light can be identified into the specific vibration modes (see figure 2.7) [24][27].

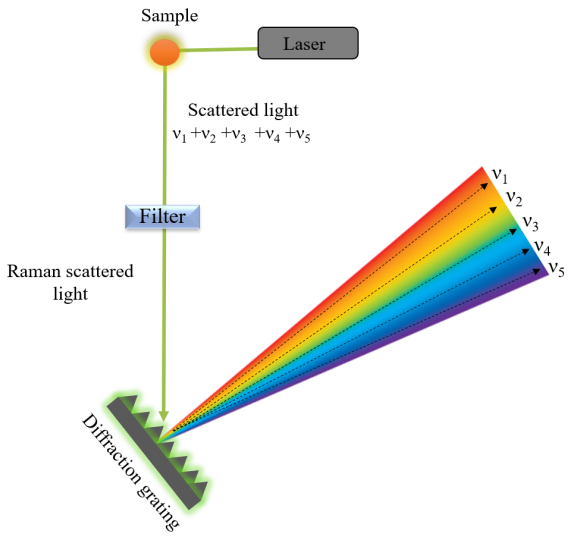

Figure 2.7: Schematic illustration of the separation Raman scattered light by the diffraction grating

4. Detector

The detection and the amplification of weak Raman signals is a severe problem that needed to be improved in the system. With the development of laser sources, the detection techniques of Raman signals have been shifted from time-consuming photographic detection to photoelectric devices such as photomultipliers (PMT), photodiodes (PD) or charge coupled devices (CCD). The collecting Raman signals from PMT can be processed either direct-current amplification or a photon-counting method. The main disadvantage while working with PMT is being time-consuming when long scanning required in spectroscopy since PMT process the photons over a broad range of wavelength simultaneously. Hence, Raman is usually equipped with charge-coupled devices (CCD) because a complete spectrum can be obtained in a shorter data acquisition time with higher sensitivity. The multichannel photon detectors like CCD are made of small photosensitive arrays where optical images can be converted into a charge pattern so it is read as a spectrum.The series of pixels arranged in both rows and columns as in the figure 2.8.

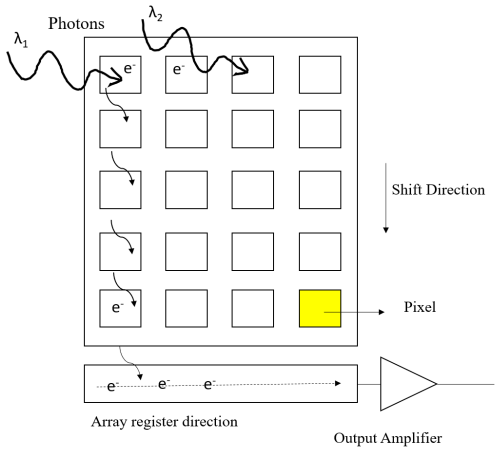

Figure 2.8: Operation mechanism of the charge coupled devices (CCD)

The size and the separation between of the pixels are defined the resolution of CCD. The arrangement of each pixel in electrodes is aligned in a way that the photons with different wavelengths can be transferred to the downwards shift direction. While photons flow through the array register direction and at the end of the readout register where the value of each charge is converted into a voltage, each pixel out of the CCD can be measured. Compared to other multichannel detectors, the readout noise during the charge-transfer process is relatively low in the CCD. Therefore, working in high quantum efficiency and sensitivity in a wide wavelength range can be performed easily. Since the Raman signals are quite weak, to be able to reduce dark current, CCDs are preferred to use with nitrogen cooling at around 130^oC [22][25].

Clearly understood from the functions of the aforementioned components, each individual component has a significant role in spectral resolution. The spatial resolution of the diffraction-limited Raman system is mostly dependent on the wavelength of the light source. However, in the case of *spectral resolution*; *the detector, the pinhole or the slit, the diffraction grating, and the distance between the detector and the grating* can be quoted as responsible factors for resolution. As mentioned earlier, the total wavelength range of the spectrometer can be determined by the diffraction grating. The higher dispersion and the better separation of the wavelength are obtained with the grating which has more lines (grooves) per mm (1/mm).For instance, 1200 1/mm is the commonly used grating which provides a wide spectral range with a satisfactory resolution. While 1800 1/mm grating can be used for high resolution, a 600 1/mm grating can be used for an average resolution which is around $1cm^{-1}$. The smaller pixel of the CCD gives the higher spectral resolution, for this reason, the function of the detector is very critical in the determination of the size and the number of collected points. In addition to this, narrow slits can provide optimum resolution when enough light reached the detector.[25].The pinhole size is very important in confocal imaging which requires both higher signal and depth resolution.

Typical pinhole size is in the range of 10 to 100 μm, therefore the lateral position of the pinhole must be aligned with micrometer precision. Since the multi-mode fibers act as a pinhole in the confocal system, by changing the core diameter of the fiber, the size of the pinhole can be easily changed to obtain better resolution in both lateral and depth [26]. For example, when working with a 100X objective; having 0.9 numerical aperture and at 532nm, the maximum pinhole size should be 50µm and 10 µm for both maximum depth and lateral resolution respectively. Because only 1 in 10^{-6} of the scattered photons belong to weak Raman scattering for image generation. While working with Raman microscopy, to fulfill the experimental expectations one always has to find a compromise between the collection efficiency and the highest resolution. From the figure 2.9 the effect of the pinhole size on the collection efficiency can be seen[26].

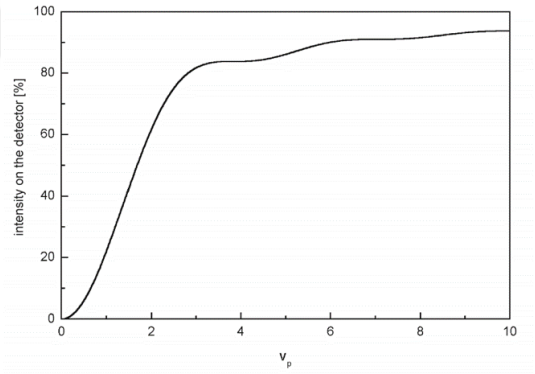

Figure 2.9: The intensity on the detector as a function of pinhole size normalized to the total power of an image plan.Image extracted from [17]

To sum up, the conventional Raman spectroscopy can give useful information about the chemistry and structure of the materials, but in the case of the implementation of this technique on the nanoscale, the measurements suffer from spatial resolution. According to the wave theory of *Abbe*, the classical optical microscopy is limited in resolution and this well-defined limit cannot be gone beyond that by conventional microscope lenses. As shown in equation (2.1), the resolution more than 250 nm cannot be obtained with the conventional oil-immersion light microscope in the visible range because of *the diffraction limit of the light*. However, the far-field ranges are quite large for the applications of nano and biotechnology. With the increasing demand for imaging the materials in the nano range, the performance of Raman spectroscopy needed to be improved to obtain the measurements with maximum molecular sensitivity and spatial resolution. When the conventional non-destructive Raman system is turned to the near-field Raman concept, the structural, chemical, and optical information of the materials can be combined with topographic information scanned in sub-diffraction like 10nm-length scales.The only way to build a high-resolution image is possible by keeping an aperture probe close to the sample surface during scanning so the scattered lights can be collected point by point and contribute to image production. The main difference between near-field and far-field Raman comes from the polarization components. While the near-field range has all three polarization components in the direction of x,y, and z, the only transverse direction is available in the far-field.Thus, without changing the position of the sample or the polarization of the source, the different polarized Raman modes emerge into the near-field region[28]. This advantage of the near-field Raman imaging can be understood from the effect of chemical treatment on the exciton emission of $1L - MoS_2$ which obtained with 80nm spatial resolution[29].Also, it has been demonstrated that near-field imaging and spectroscopy can directly visualize the structural features and the emission profile of excitons of the $1L - WS_2$ with around 70nm spatial resolution[30].The details of *the Near-field Raman Spectroscopy measurements* can find in the Appendix section.

Chapter 3

Results and Discussion

3.1 Scanning Photocurrent Microscopy to understand the photocurrent generation mechanism of Silver Nanowire

3.1.1 Silver Nanowire

Compared to the bulk counterparts, the outstanding properties of the one-dimensional (1D) metallic nanostructures have been taking attention for the last decades. The optoelectronic properties of metallic nanowires strongly depend on the size of nanowires. As having at least sizes between 1 and 100 nm in dimension, demonstrate interesting optical, electrical, magnetic, and thermal properties due to the confinement effect. When the size of the nanowire gets close to its electron mean free path, the resistivity of the nanowire increases due to the surface scattering of electrons. Although smaller diameter nanowires are less stable environmentally, they are advantages in terms of optical transmittance in optoelectronic applications. In an opposite way, when the diameter of the nanowire

increases, scattered photons amount from the surface increase and result in decreasing transmittance in the thin film. However, in terms of having fewer junction points in the unit area, longer nanowires are beneficial to improve the optical transmittance.[31][32]. Among other metallic nanowires, the silver nanowire is the most preferred nanostructure due to its physical properties [33].Along with having the characteristics of one-dimensional materials, the silver nanowires hold high electrical (6.39 S/m) and thermal conductivity(429 W/(m·K)) properties as inherit from the silver. Hence, they are highly preferred in the applications of solar cells, touch screens, flexible sensors, and electromagnetic shielding [34][35].

Figure 3.1: Application areas of Silver Nanowires.Image extracted from [20]

Not only the single nanowire itself, but also the network of silver nanowires catch attention due to their such properties as high flexibility, optical transparency, bending, and stretchability performance[34]. The unique properties of silver nanowire networks stem from the creation of conductive pathways inside the random network. As based on the 2D percolation model, the conductive pathways are created by linkage of the individual nanowires, hence increase by increasing nanowire network density. Since the linkage of nanowires opens a path that can electrons flow, the conductivity also increases by an increase in network density[36] (see Figure 3.2).

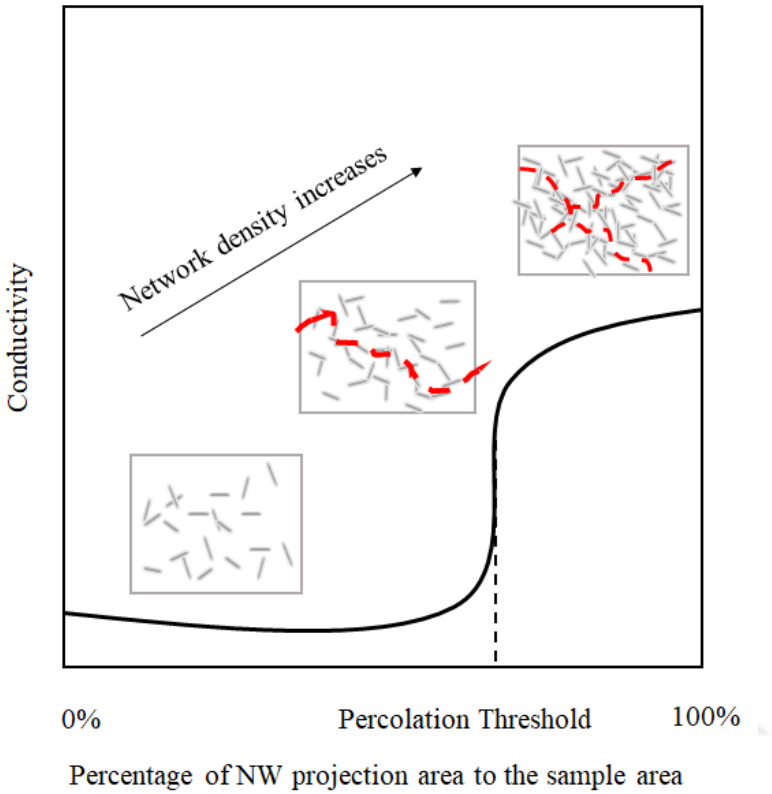

Figure 3.2: Conductivity versus percentage of NW projection area to the sample area

As it can be seen in figure 3.2, in the percolation threshold the nanowires tend to coalesce and form intersections in the network. The network density and also the carried current flow change after passing this threshold, therefore the low sheet resistance is obtained, however, this effect decreases the transmittance. On the other hand, the length of the nanowire has an impact on the shift of the percolation threshold. Therefore, higher conductivity can be obtained with longer nanowires at a lower percentage of nanowire projection area to the sample area[31].

The synthesis of AgNWs is an inexpensive method.The most popular and commonly used synthesis method is the polyvinylpyrrolidone (PVP)- assisted polyol process. In this method, the reduction of silver nitrate ($AgNO_3$) with ethylene glycol (EG) takes place in presence of PVP. It is believed that the use of PVP and the introduction of the seeding agents are the keys to the formation of uniform silver nanowires. Therefore, sodium chloride (NaCl) is added to the solution to prevent the agglomeration of the Ag^+ when in the initial stage of Ag seed formation. While dissolving the AgCl solution in the late stages of the process, releasing of Ag+ ions into the solution take place. At this stage, the morphology of the silver nanowires can be controlled by the additive of PVP [37].For example, the addition of low concentration PVP to $AgNO_3$ solution decrease the PVP encapsulation on nanowire and it leads silver nanowires grow longer. On the other hand, high-concentration PVP amount in the solution may result with the isotropic growing which leads to synthesis of shorter nanowires[38]. However, the encapsulation of the nanowires with the insulating surfactant, PVP, layer increases the contact resistance between nanowires and causes instability in electrical conduction and degradation in the overall device performance[34][39][40]. Such treatments as thermal annealing [41][42], plasmonic welding[43], bending[44],mechanical pressing[45], solvent washing [46][47], electron-beam irridation[48] and plasma treatments[49][50] are applied on the Silver nanowire networks to decrease the contact resistance. The preference of the treatments mostly depends on the properties of the nanowires and the application area.

Figure 3.3: PVP effect on nanowire resistance.Image extracted from [35]

The deposition of the nanowires is the first important step in device fabrication. Vacuum filtration, rod deposition, spray coating, or drop-casting are just some of the easy deposition methods[40]. According to the application area, the deposition of nanowires is performed on different substrates such as polyethylene terephthalate (PET)[51][52], glass [46][53], SiO_2[54][55], and sapphire [56].

3.1.2 Device Fabrication

In this study, the single silver nanowire and the network of silver nanowires were prepared by using the drop cast deposition method. Although there are some advanced methods to prepare the nanowire networks like using the grating lithographic patterning method[57], as it is presented in this work, the successive drop-casting by using a diluted solution is also enough to obtain a well connected nanowire network. The accumulations of nanowires and polymer residues on the substrate can be seen in figure 3.4.To be able to obtain a separated and also well-connected nanowire network, the density of the nanowire solution is very critical in the drop cast deposition method.

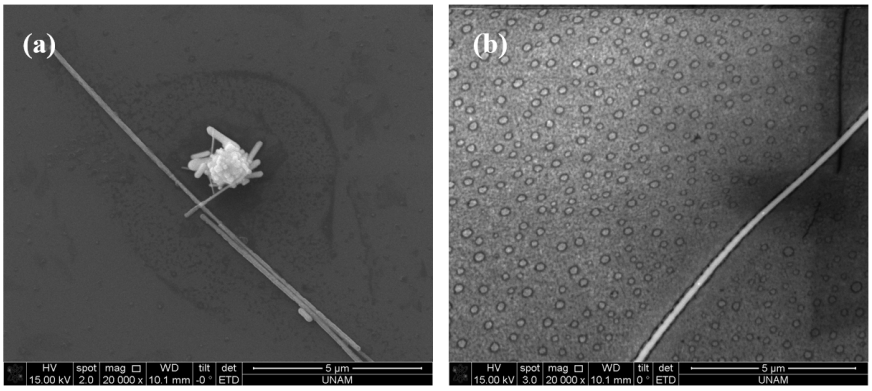

Figure 3.4: (a) Accumulated nanowires; (b) Polymer residues on substrate

For this reason, the purchased silver nanowire suspension (Sigma-Aldrich with the average diameter and the length of nanowires are 120-150 nm $\times$ 20-50 μm respectively) was diluted by mixing 20ml isopropyl and two drops of nanowire suspension. Also the crystal structure and the presence of PVP can be seen in the following XRD and Raman results respectively.

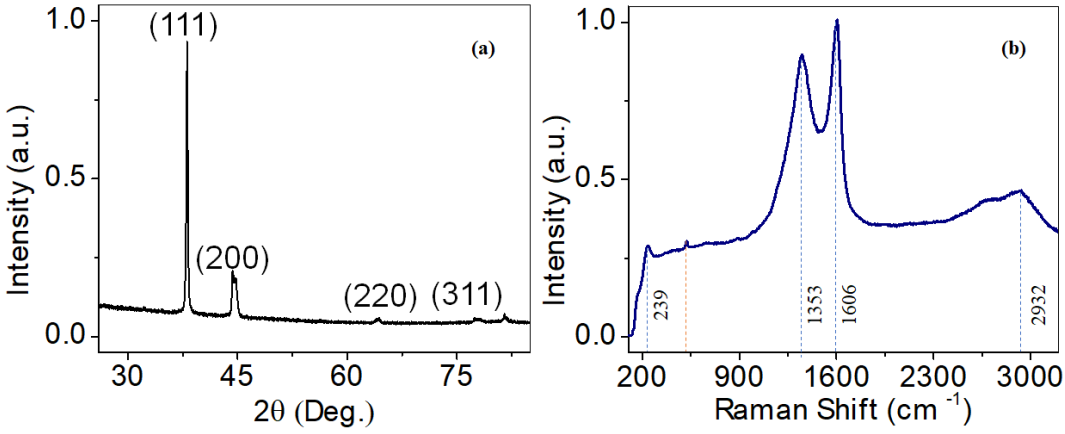

Figure 3.5: (a)XRD pattern of Silver nanowires confirms that the FCC crystal structure (b) Raman spectra of the silver nanowires covered by PVP

The dilution process of the nanowire suspension is a very important step in the device fabrication process to be able to obtain both a separated single nanowire and also the connected nanowire networks. The next step is the deposition of the nanowires. The drop-casting of the diluted solution was performed by using a Pasteur pipette onto the clean two-side polished sapphire substrate. As it can be understood from the experimental demonstration in the figure 3.6, placing the indium contact was done right after the air drying of the drop-casted suspension.The soft metal indium was melted around 170 ° C on the hot stage and with help of a nanomanipulator, the sharp indium needle was formed by dragging from the bulk melted indium source. The formed sharp indium needles were placed on both sides of the Silver nanowire to work as a contact in electrical measurements.

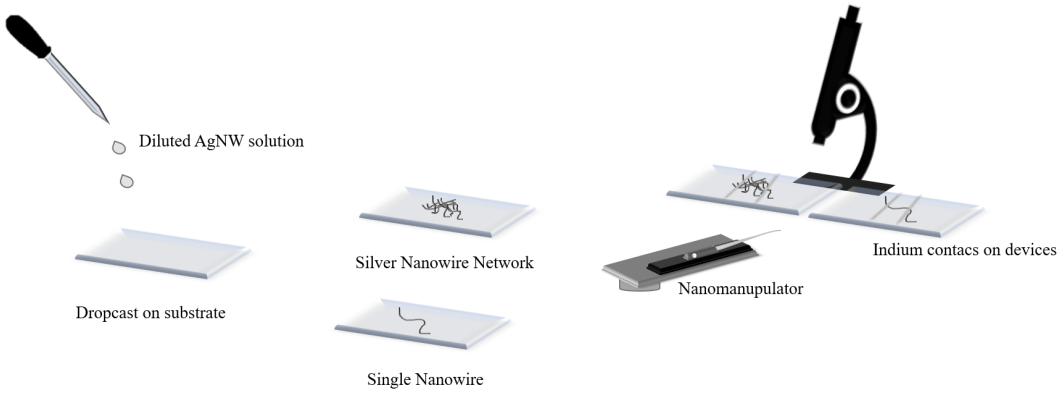

Figure 3.6: Device fabrication with indium contact

3.1.3 Photocurrent Mechanism

The photocurrent mechanism in silver nanowires is considered based on two contributions: the photo-bolometric effect as discussed in chapter 1 and the role of the surface plasmon polaritons on photocurrent generation.

- The Role of Surface Plasmon Polaritons

The outstanding optical properties of metallic nanowires are attributed to the plasmonic effects. This is also the reason why plasmonic technology aims to control the surface plasmons of the materials. The electrons polarize and oscillate when the metal surface irridates by an electromagnetic radiation. The interaction between electromagnetic radiation and the free electrons creates plasmonic effects. Such metal nanostructures as Ag, Cu and Au exhibit surface plasmon resonance light absorption in the visible spectrum[64]. Especially AgNW networks serve as a high performance plasmonic nanostructures for optoelectronic devices due to the enhancement of light-trapping and light-scattering effects[65]. Howevever, it is necessary to add an extra momentum on photons to be able to launch the SPPs in metallic nanowires. For this purpose, different coupling strategies such as by electron exitation [66], evanescent coupling [67], local scattering[68],fluorescence coupling [69], using an optical antenna[70],and waveguide excitation[71][72] are developed to launch SPPs in nanowires. As it is depicted in the figure 3.7, once the surface plasmons are coupled to the photons, the created electromagnetic waves propagate along with the interface which is called surface plasmon-polaritons (SPPs). The electromagnetic field is confinded the near-vicinity of the interface and decays exponnantially as perpendicular to interface [73].

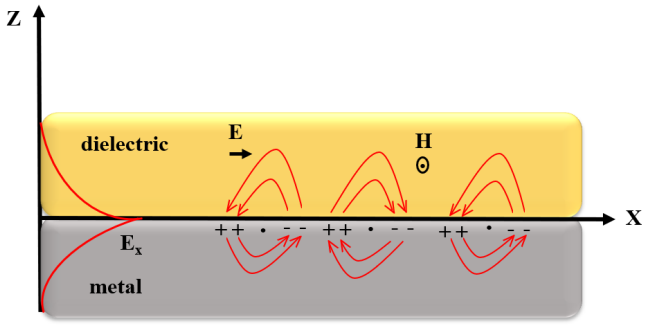

Figure 3.7: The electric and magnetic fields distrubutes around the propagating SPPc in the interface of metal and dielectric.

3.1.4 Results

Once the laser light focuses on the sample, the voltage bias is applied through the indium contacts according to the capacity of the type of the device. While the single nanowire can bear maximum of 10mV bias ranges, the network devices can bear values in a hundred millivolts ranges or more bias value due to the forming of the conductive pathway in the network structure. As depicted in figure 3.8, laser light starts to scan over the network region between the indium contacts with a specific step size to collect the photocurrent contribution of each data.

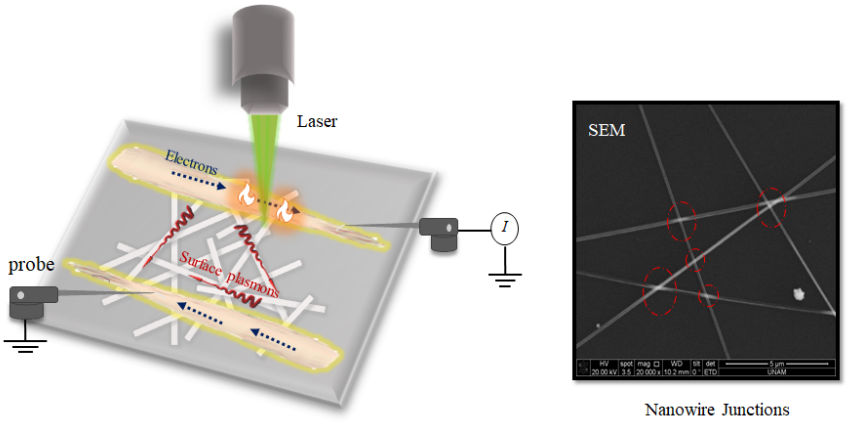

Figure 3.8: Focused laser light scans over the network sample

Meanwhile, the current flows through the source and drain contacts. At that moment, the focused laser light also excites and launches the surface plasmons polaritons by supplying an additional momentum, thus SPPs start propagation through the junction points. The electric field intensity intensifies at the junction points by accumulations of propagating SPPs. While SPPs energy mostly absorbed by the nanowire causing a rise in temperature and change in resistance. Therefore, the photocurrent generation based on the bolometric effect that emerges with the existence of SPPs propagation is observed.

The current-voltage behavior of each prepared sample was checked before performing photocurrent measurements. The following figures demonstrate the resistance of the devices and the photocurrent maps under different bias conditions.

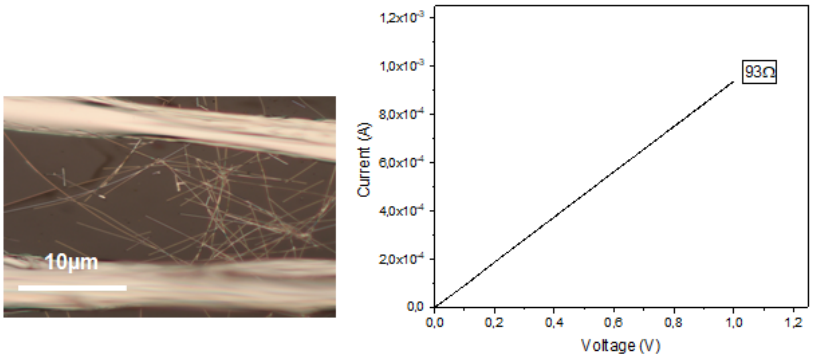

Figure 3.9: Optical microscope image of the network sample 1 and its I-V curve

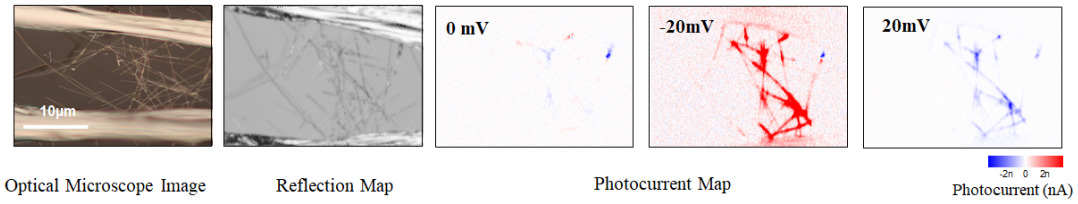

Figure 3.10: Reflection and Photocurrent Maps of the network sample 1 under zero bias at 126μW laser power, 20mV and negative 20mV bias at 108μW laser power

The network samples consist of the connection of several individual nanowires, however, each nanowire can not contribute to the photocurrent generation because of the possibility of having a weak network connection or nanowire surface inhomogeneity. Here is an SEM image that clearly shows the contribution of individual nanowires on a photocurrent map.

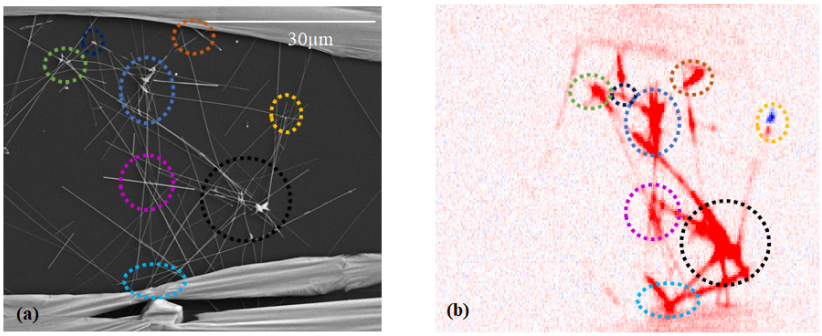

Figure 3.11: The contributions of individual nanowires on network photocurrent map

As it can be seen in the next results, along with dense networks, single nanowires and less dense networks were used to fabricate devices on sapphire substrates.

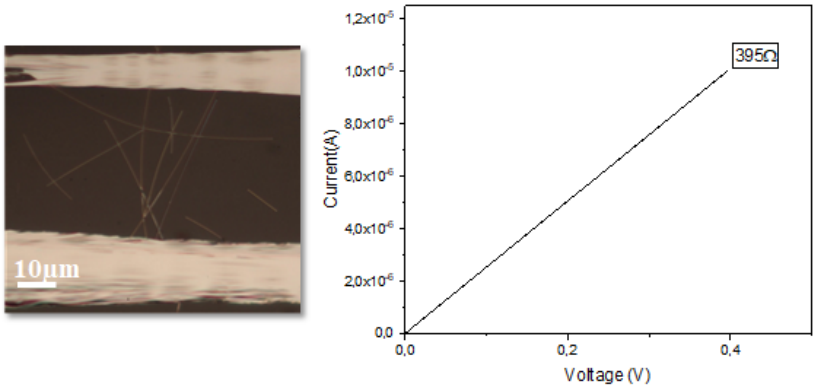

Figure 3.12: Optical microscope image of the network sample 2 and its I-V curve

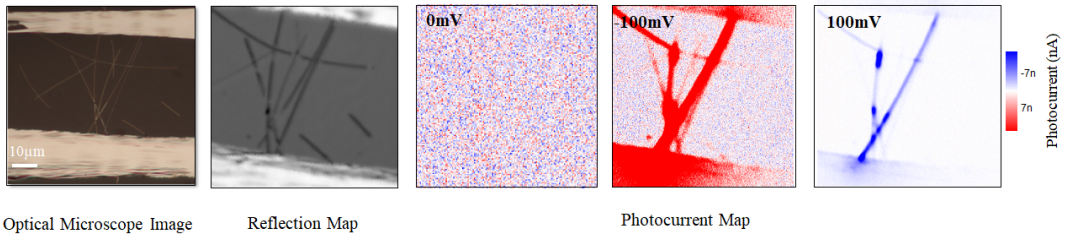

Figure 3.13: Reflection and Photocurrent Maps of the network sample 2 under zero bias at 131μW laser power, 100mV and negative 100mV bias at 109μW laser power

The applied bias and the laser power were kept minimum during the photocurrent measurement of the single wire device since excessive values may result in device explosion.

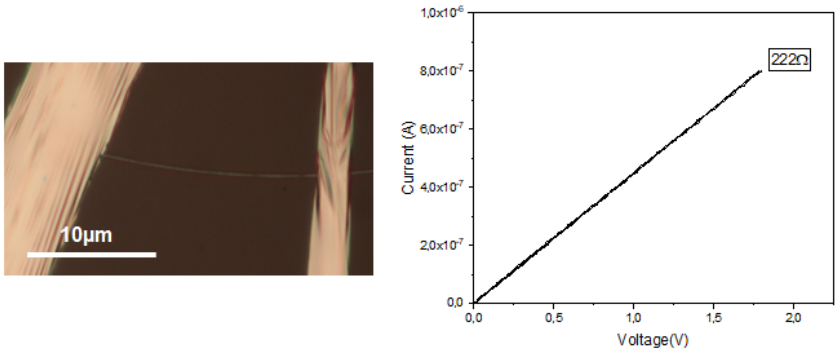

Figure 3.14: Optical microscope image of the single nanowire and its I-V curve

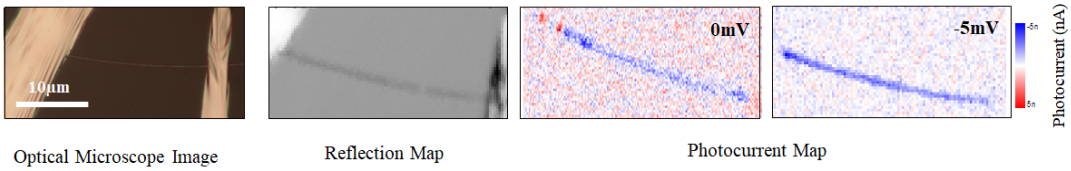

Figure 3.15: Reflection and Photocurrent Maps of the single nanowire under zero bias at 140μW laser power and negative 5mV bias at 52μW laser power

Network sample 3 was prepared on a soda-lime silicate glass substrate to be able to see the effect on photocurrent generation.

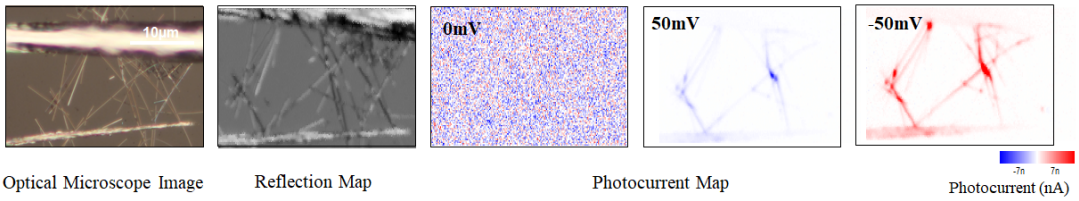

Figure 3.16: Reflection and Photocurrent Maps of the network sample 3 under zero at 138μW laser power, 50mV and negative 50mV bias voltage at 108μW laser power

In the scope of these results, the proposed photocurrent generation mechanism can be concluded under the following considerations. First of all, the sign of the generated photocurrent reflects effects of homogenous heating with change in resistivity of device. In addition, the signal generations are observed over the indium contacts which is an indicator of the contribution of SPPs on photocurrent generation.On the other hand, some signal variation can be attributed to laser heating-induced local oxidation of nanowires. When there is nanowire diameter shrink below 100nm, high-surface to volume ratio makes nanowires vulnerable to surface corrosion [36].Therefore the network conductivity and signal generation fails. Finally,it should be noted down the intensify signal generation comes from the junctions point in the network device.The density of the network is a very effective parameter on the amount of resistance the device shows and also the possibility of survival of the device under applied different voltage bias and laser power are strongly related to this.

3.2 Raman Spectroscopy for the analyzing the glass defects

3.2.1 Structure of Glass

The usage of glass is dated back to around 3500 BCE in Mesopotamia, however, the development of glass technology on large scale for different types of glasses were started mostly in the 14th century. Because of the broad range of glass types, these materials were able to catch attention for usage in different applications. Therefore, they could be categorized and had a place in different groups as ionic melts, metallic alloys, aqueous solutions, polymers, and molecular liquids. Glasses are inorganic materials and have an amorphous structure that does not have periodicity in the crystal structure. Even some other materials like organic polymers have an amorphous structure, but they can not be included in the family of glass [74]. To understand the glass formation based on structural properties, Goldschmidt's theory (1926) is the earliest study in the field. According to theory, the radius value in oxide glass plays a critical role in building the structure of glasses. According to the theory, the value which can be obtained by dividing the radii of the anion (rc) to the radii of the cation (ro) is between 0.2 to 0.4 for all glass-forming oxides. SiO_2 and GeO_2 glasses can be examples to support Goldschmidt's theory, however, the overall theory is weak in terms of explaining the bond types and relations with oxides. To extend the understanding of glass structural formation, Zachariasen studied further on Goldschmidt's' theory and formulated the glass formation rules which are named with his name. He put forward the idea of the small radius ratio in Goldschmidt's theory represents the low coordination number. Those which have an open structure should be the source of creation of a disordered structure in glasses since there is no requirement of sharing neither edges nor faces by the polyhedra coordination. If it is not the case, then crystallization, an ordered structure is created. In addition to these, Zachariasen declared that both the glassy and crystalline forms of the glass oxides could not have many big differences in their energies because in both states the mechanical properties show similarity.

Only the higher energy of the glass could lead crystallization to take place in the structure[75]. Therefore, Zachariasen formulated his thoughts on four rules of oxide glass formation as a theory. The first rule says that the cation coordination numbers must be small. Secondly, it says that there is no linkage with more than two cations for an oxygen ion. It is explaining in the third rule that not edged or faces, only corners are places to share for oxygen polyhedra. The final one concludes that to create a 3D network, the number of corners in an oxygen polyhedron shared by another polyhedron must be at least three. The four rules aforementioned are valid for the RO_2, R_2O_3, R_2O_5 types of oxides. For example As_2O_3, P_2O_5, GeO_2 and SiO_2. These examples are given for the glass which is made of one oxide system, However, glasses are not only made of one oxide. They can also consist of binary systems and several components. $R_2O - SiO_2$ can be an example for the binary-system, R is a representative alkali[76].

When the crystallization states deteriorate with the variation of the R-O-R bond angles, a random network of oxygen polyhedra forms. From the similar structural point of view, highly ionic compounds such as MgO, TiO_2 and Al_2O_3 are not considered as good glass formers since the edges and the faces of oxygen polyhedra are forced by long-range colombic interaction. According to Zachariasen rules, tetrahedral SiO_2 and triangular B_2O_3 are well-suited glass formers since they have both covalent bonding, and easily build the corner shared networks. In figure 3.17 demonstrates the crystalline and the glassy structure of R_2O_3[75]

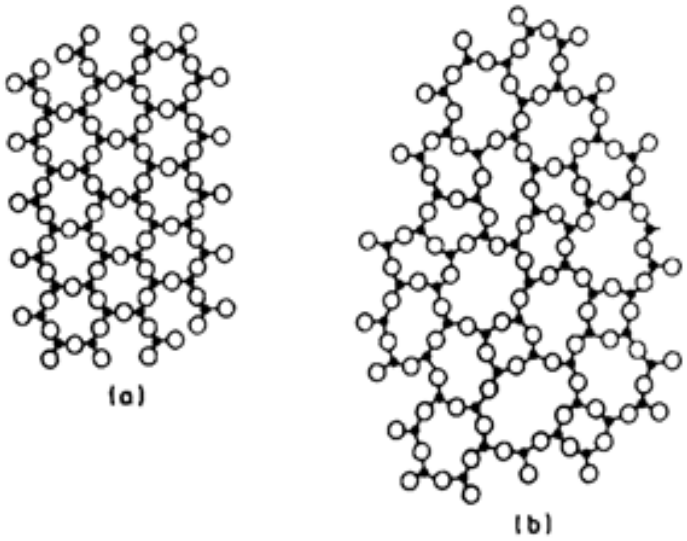

Figure 3.17: (a)Crystalline structure (b)Glassy structure of R_2O_3

Glass network formers are such as SiO_2,P_2O_5,and B_2O_3 are like backbone of the glass structure, held a significant role in glass formation. According to the Pauli Scale, the best network formers in the glass structure have electro-negativity values in the range of 1.70 to 2.1. Another important role is attributed to alkali oxides called as network modifiers in the glass formation. These materials can modify the properties of the glass since they can be activated thermally. This activation results in the movement of alkali metal ions in the glass structure. By this movement, alkali metal ions exchange their place with the other ions near to glass surface.Al_2O_3, PbO, CaO, SrO, Cr_2O_3, Li_2O,K_2O,Na_2O, BaO, CuO, MgO and Bi_2O_3 can be given as examples of network modifiers.[77].

The behavior of network modifiers can be understood in the following example. The figure 3.18 demonstrates the 3D tetrahedral network of SiO_4. The oxygens in the tetrahedra are shared by neutral SiO_2 units as $[SiO_{4/2}]^0$. The superscript zero in the abbreviation of unit implies the charge.[75]

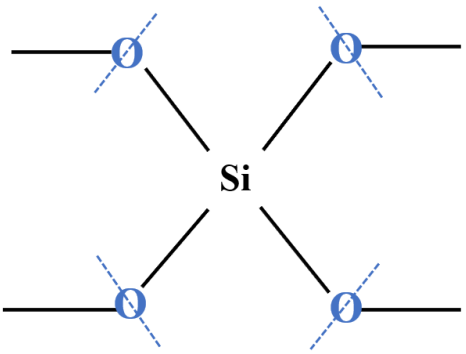

Figure 3.18: Tetrahedral network of SiO_4

There are dashed lines across the oxygen symbol in the network, this means that oxygens are shared between tetrahedra. So, Si-O-Si linkages occur in the glass. In case of adding an alkali ionic oxide network modifier like $Na_2O(2Na^+ + O)$, to SiO_2, following reaction which is shown in the figure 3.19 takes places between them;

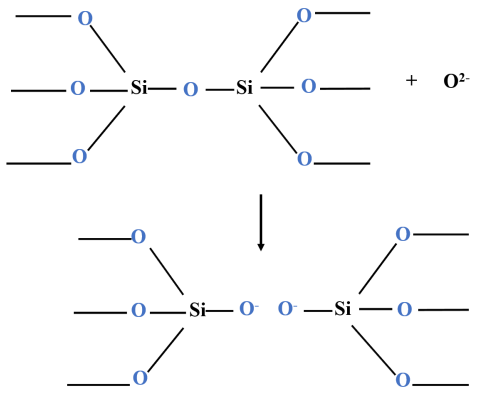

Figure 3.19: The reaction step after adding Na_2O to glass batch

This reaction can be shortly written as;

$$2[SiO_{4/2}]^0 + Na_2O_2[SiO_{3/2}O]^- + 2Na^+ \tag{3.1}$$

The effect of the Na_2O network modifier on the system can be see clearly in this reaction. Na_2O breaks the bridging oxygen between Si-O-Si in the structure therefore eliminates the Si-O-Si linkages and then form a new linkage between Si and non-bridging oxygen as in the form of Si-O[75]. Glass network modifiers can be categorized into three different groups; Flux agent, Stabilizers, and Colouring ions. The first group consists of alkali metal ions such as Na and K, they play role in lowering the melting temperature of the glass batch. Like Ca and Mg, alkaline earth metals are part of the stabilizer type modifiers and they can be used to stabilize the glass composition. The last group is responsible for the physical appearance of glass. By adding the metal oxides and such metals like Fe, Mn and, Cu into the glass batch, the Si-O bridges and also the connection between glass networks are distorted which resulted in the changing in chemical and physical property change in the glass [78]. In general speaking, to define the crystal structure of materials, there are some key features of materials that need to consider such as the lattice types, unit cells, position of atoms, and the special symmetry they have in the structure. In the case of amorphous glass, it is not possible to talk about the presence of translational symmetry and lattice structure. For these reasons, glass structures are required to analyze by different approaches. The most used approach to define the structure of glass is considering the degree of orders. This term can be divided into three categories: Long-range order, intermediate order, and short order. In the short-range order, the radial distance between the structural blocks is around 2Angstrom (Å). On the other hand, intermediate-range order and long-range order have the radial distance less than 20 Å (10 -20 Å) and more than 20 Å respectively.[79]. The following the figure 3.20 demonstrates the physical parameters to define both short and intermediate-range order glass structure.

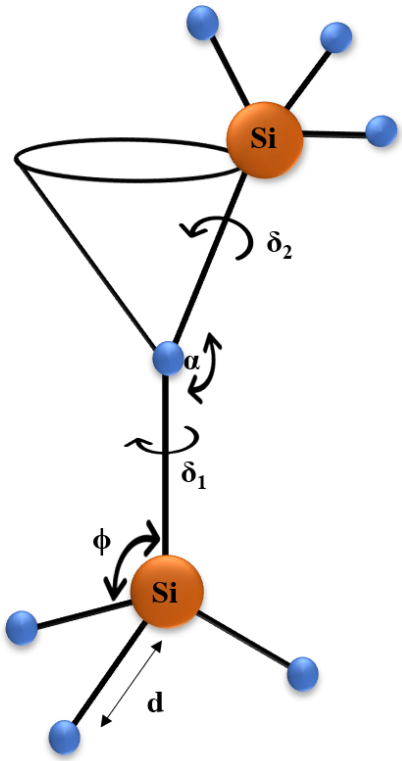

Figure 3.20: The parameters to define the short-intermediate or long-range order of the glass; d:the bond lenght,ϕ :the tetrahedral bond-angle,α:the bridging oxygen bond-angle,δ_1 and δ_2: the bond-torsion angles

In addition to structural order classification, another important approach to defining the glass is linked to the thermodynamic properties of glasses. The following figure 3.21 summarizes the thermodynamic equilibrium condition of a glass structure.

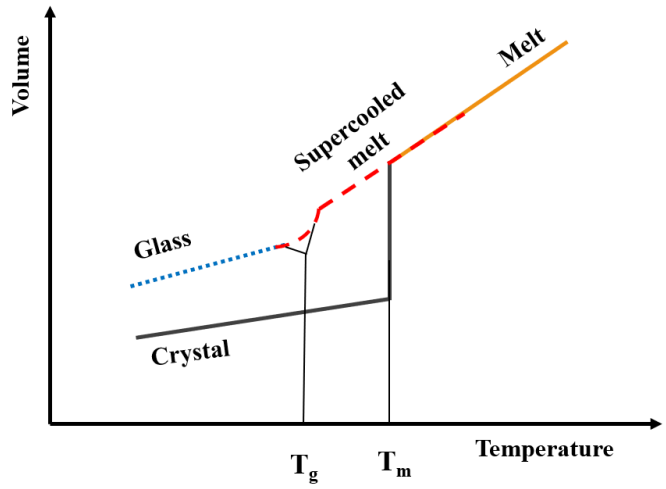

Figure 3.21: The plot of the temperature dependence versus volume

Once an ordinary liquid or melt cooling down, there is a decrease observed in its volume because crystallization takes place at the melting point of the liquid. When the temperature is keep decreased, a further decrease is observed in the volume since the expansion coefficient of the crystal is lower than the liquid. However, in case of no crystallization at Tm, the volume keeps decreasing along the area which is called supercooled melt or liquid. As a result of this condition, a metastable- thermodynamic equilibrium region exist. As it can be seen from the figure, the curve which represents the metastable equilibrium follows a similar parallel behavior with the crystal curve. The reason behind following a parallel path by showing deviation is related to increase in viscosity of the liquid during cooling. Reaching the equilibrium of the liquid takes place very slowly in meanwhile the viscosity becomes so high that continuous cooling can not be enough to reach the equilibrium anymore. The best way to describe this continues temperature change which is the indicator of viscosity, it to call as glass transition temperature, Tg. Therefore, it can be concluded while below Tg value glass is considered as a solid material, above Tg it is a melt [76]

3.2.2 Glass Bubble Defects Formation Mechanisms

The glass production process consists of different steps which each of which takes place at a different location in the production line. During the process, both raw materials and also shaped glass may encounter adverse conditions and this can end up with defect creation in the glass structure. These defects have to be eliminated from the structure since they can reduce the mechanical strength of glass by creating stress on the body, damage the optical homogeneity and misfunction during usage. Not just because of deterioration in physical properties, also from economic aspects, defects are undesired since they reduce the efficiency in the production process and lead to a loss in revenue. In the figure 3.22 shows the inside structure of a production unit; numbering points out the locations which may be the possible sources of defects[80].

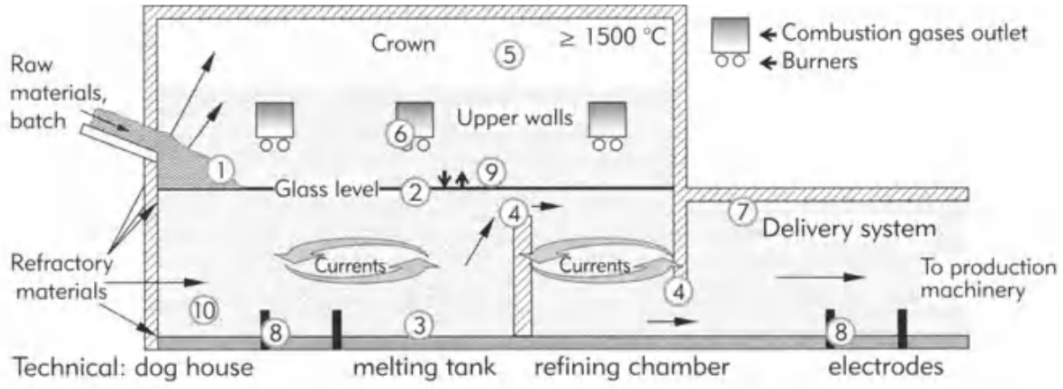

Figure 3.22: The schematic illustration of a production unit.Image extracted from [40]

The first step in the production line starts with the preparation of raw materials. The sand is as a glass network former, and recycled glass cullets are firstly preferred raw materials in terms of efficiency in the process. Also, the network modifiers and fining agents are added to the glass batch to improve the process by increasing the melting rate and remove the gas bubbles during melting, respectively. The glass recipe is prepared according to the desired type of glass. For example, in the production of borosilicate glasses, borax and boric acid are used as raw materials.[81] The grain size, degree of purity, water amount, the potential pollution level to the environment, the behavior in the melting stage, and by considering the total cost of the raw materials in the process are chosen carefully. However, these precautions generally cannot eliminate defects from the product completely [80]. In this stage, the reaction between raw materials and the batch refractory materials such as AZS (Al_2O_3-ZrO_2-SiO_2 fused-cast refractory) or chromium oxide blocks may lead the creation of defects[81]. In second step, raw materials are faced with three environment conditions: refractory effects, glassy state and atmosphere. Here is the step which Knot types of defects are often formed[80]. Knots are known as transparent stones since they have an opaque appearance. They can form in different sizes on the wall of bottles. The third possible defect source location is the surface of the melting tank. Before reaching the melting stage, the fining agent is added to the glass batch to remove the bubbles but in the early stage of the melting process, bubbles are desired because they play role in the homogenization of the batch. However, they are needed to be eliminated before the refining stage which is one important step prior to shaping the glass, to prevent further interaction between bubbles and the rest of the glass composition.[81]. In the bubble type defect, the final glass product has circular or hollow spaces which keep the different type of gas amount inside. Oxygen, argon, carbon monoxide, carbon dioxide, hydrogen, sulfur dioxide, chlorine, fluorine, nitrogen or combinations of different gases can be given as examples of gasses inside the bubble defect[82]. In third stage of production unit and the rest following units are creating some more conditions to create bubble defects.

The formation of bubble defects can stem from these conditions; decomposition of the batch materials, reaching the supersaturation of the melt, both electrochemical and chemical reactions, refractory contaminant materials, and mechanical stirring of the batch[83].In the step four and five is under attack of ion exchange which lead the corrosion and abrasion effect by glass flow. Also, at step six, the accumulation of both combustion gas and the volatilization of some batch component may create defects. When volatile components reach to step seven, interaction of gases with refractory materials may result as the localized corrosion at pores of refractory furnace. Step eight and nine create a perfect environment for the creation of bubble defects by using metal electrode heating and the exchanging the gases between glass and the atmosphere, respectively [80].In case of metal electrode heating, bubble formation can be seen on thermocouples or metal electrodes. While one metal part of electrode is in contact with glass melt, the second electrode is generally created by a refractory. At high temperature glass melt act as an electrolyte, in case of short circuit connection between both electrodes, an example galvanic cell mechanism are created, and following reaction takes place on the anode [83]:

$$2O^{2-} - 4e^{-} \leftrightarrow O_2(g, l) \tag{3.2}$$

The last step in the production unit include metallic inclusion and stones types of defects. Stone defects are like large crystalline inclusions. They can be form by crystallization reaction between refractory materials or undissolved raw materials. Metallic droplets originate from the melting unit or as a result of different chemical reaction, for example the reduction process in the glass melt tank. Therefore, when electrode materials are affected both chemical or physically, metallic inclusions releases into the glass as defect[82]. Finally, formed glass moves towards the analysis part in the production line to identify the possible source of defects in the product. The following seven effects are needed to be considered to investigate both the gas amount and type inside the bubble and also to understand exactly at which location bubbles are started to emerge [84].

1. *Incomplete fining processs*

   The fining or refining process involves two important mechanism in the removel of gases inside the molten glass. The first mechanism is buoyant effect. The second mechanism is the dissolution of bubbles. In this step, the furnace temperature, glass viscosity, exposure time and kinetics of environment affect the efficiency of the fining process. When raw materials enter the furnace melting tank, the temperature is generally high enough and the viscosity of the glass is low to allow buoyancy forces to remove the bubbles which sizes are greater than 1mm. However, when raw materials are exposed to inadequate temperature flow, the viscosity of the glass becomes too high, this situation results in the rise of the bubbles which sizes are smaller than 1 mm, called seeds. The second mechanism plays a role the remove the seeds from the molten glass. As the molten glass cools down, gases start to dissolve in the glass since the gas solubility increases. Here, time is a very critical factor. Incomplete fining process time may destroy these mechanisms to work. The molten glass needs more time to dissolve the gases until shifting to the forming unit. Na_2SO_4, $CaSO_4.2H_2O$,$BaSO_4$, As_2O_3, NaCl, CaF_2 and, Sb_2O_3 are some important fining agents which raw materials batch has to be added to glass batch to let bubble removing mechanism works[85].For example, in the case of adding Sb_2O_3 into the glass batch, the absorption of bubble takes place in following reversible reaction since the temperature has both supportive and suppressive effect on the bubble formation[86].

$$Sb^{5+}(l) + O^{2-}(l) \leftrightarrow Sb^{3+}(l) + 1/2O_2(l,g) \tag{3.3}$$

2. *Contaminant*

   The cullets are added to the glass batch to decrease the energy consumption in the process, however, the addition of cullets may lead to an increase in bubbling since their melting contributes to the creation of a viscous melt which may react with the raw material batch. For example, the CO_2 bubble in the glass could be a result of the addition of carbide cullets to the batch [86].

3. *Entrapment of air*

   The glass batch is mechanically stirred by applying pressure, as a result, excessive movements inside the batch mixture may lead to the creation of trapped air in the glass[85].

4. *Reboil Effects*

   The bubble creation can easily take place in the inhomogeneity of the glass batch since the gas supersaturation is triggered by some external stimuli in the melt. These different stimuli are defined as reboil in glass technology. Reboil effects can be classified as compositional (i.e. the basicity of the glass melt), chemical (i.e. fining agent reaction with the atmosphere), thermal (i.e. temperature flow inside the furnace), mechanical (i.e. stirring or agitation), electrochemical (i.e. oxygen-producing reactions) or radiative (i.e. intensive radiation change)[86].

5. *Refractory Contamination*

   When the molten glass comes in the contact with the refractory materials inside the furnace walls, refractory corrosion takes place. As a result of this, the basicity of the melt decreases and CO_2 or H_2O release[86].

6. *Electrolysis Effect*

   The short-circuit contact or weak grounding issues and inappropriate electrode usage with refractories may result in oxygen bubbles generation, especially between ZrO_2/Al_2O_3 refractories and glass melt[86].

7. *Devitrification*

   The temperature instability between the furnace bottom and flowing around results in bubble formation, especially in the transition from colorful to clear glass is seen[86].

3.2.3 Identifying the impurities/gas compounds inside the bubble defects with Raman Spectroscopy

The glass production process is mainly responsible for the various types of creating on glass defects since each location at the production unit has different environmental effects on raw glass materials. However, some defects may be generated because of the finishing processes, for example inappropriate cooling cycle on the molten glass can result in having different phases in the structure which leads to the failure of the final product after some time or such hot-forming processes as drawing, floating, and pressing can create some defects near to the surface of the final product [80]. Defects are needed to be investigated by appropriate tools. While some of them can be visible to naked eyes, some defects are not possible to identify without microscopic analysis. Therefore, several methods are available for scientists to use in the analyses of bubble defects in the glass structure. The common methods [84] used in analyzing the gases inside the bubble and the reason why Raman Spectroscopy is chosen in this work can be understood as follows:

- *Light Microscopy*- The morphology of the bubble; size or shape can be observed by using different magnification objective lenses but detailed information about the gas components inside the bubbles can not be obtained through this tool.

- *Chemical Solubility* -It's an inexpensive method for detection of the closed bubbles near to bottom or top surfaces of glass. Bubble-contained glasses are submerged into such solution as glycerin, the diphenylcarbazide solution, the acidified barium chloride solution,and 10 percent of lead acetate solution to observe SO, CO_2, H_2S dissolution, detect the colorimetric agent, the sulfates, and the sulfide amount respectively. Although the test can be performed quickly and examined the glass on-site, the accuracy, which is the main drawback of the method, is sometimes less than expected in the test

- *Gas chromatography* -The main reason to be preferred this method is because of having both fast analyses and fast operation along with the easy maintenance procedure [84]. The components of this tool can be demonstrated as in the figure 3.23. The composition of the gas compounds inside the bubble is analyzed in a destructive way.

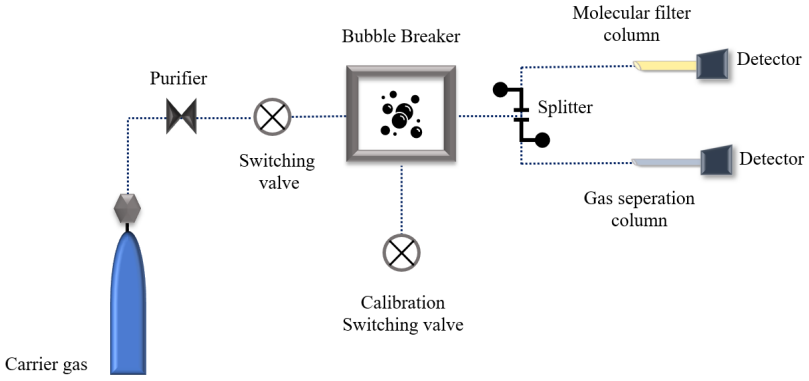

Figure 3.23: Components of gas chromatography

First, the glass is needed to be broken into pieces via crusher under the vacuum chamber and released gases are needed to flow in the presence of the high purity helium gas carrier environment to the analyses. The released gases from the bubble is separated through the gas separation column and collected with the molecular filter. The gases are separated due to their different retention times. After filtering and separation of the released gases, the gas flows to through to helium ionization detector (HID) which is the best option while analyzing the smallest gas amounts. In this method, mass-specific detection is not possible [80]. The absorbed gases on the chamber wall create a contamination problem in each measurement. Another drawback stems from the separation and detection of the argon gas which is one of the main sources of bubble formation inside the molten glass, can not be performed. Also, the measurement method suffers from the lack of sensitivity to SO_2 gas which is another important bubble source in the glass batch. [84].

- *Mass Spectrometry*-This instrument is quite useful for the analysis of the gas compositions inside the bubble since it has enough sensitivity, both resolutions, and scanning ability, also it is capable of microprocessor-controlled data acquisition and mass programming[80].Mass Spectrometers systems can be divided into two as static and dynamic. They have some operation differences such as gas-handling manifold can be controlled from the pumps in static system[84]. Compared to the gas chromatography method, the separation of argon and oxygen is not a problem, however mass spectrometry face some difficulties in differentiating between nitrogen and carbon monoxide[80] In similar to gas chromatography, the wall surface of the chamber absorbs the bases which is a contamination source. Also, the leakage of the gases from the chamber wall and the possibility of the chemical reaction that occurs between the electron source materials can be counted as the drawbacks of the instrument[80].

- *SEM/ EDX Analysis* -The morphological observation of organic and inorganic materials can be performed by Scanning Electron Microscopy analysis method. While the electron beam raster the surface of the material, this interaction results in the production of special signals such as secondary electrons, Auger electron, back-scattered electrons, X-ray, and different energy photons. SEM can be coupled with an Energy-dispersive X-ray detector (EDX), in which compositional information can be collected from the specimen. However, in the case of analyzing the gases inside the bubble, EDX analysis can be used only for the detection of the deposits in the bubbles such as selenium and sulfur[87].

- *Ion microprobe mass spectrometry*-The biggest advantage of this instrument to have the ability to analyze the small bubbles with high sensitivity by removing the absorbed gases layers while measuring. Also, it can detect the compositional variations of the glass near the bubbles, however, this instrument is quite expensive[84].

- *Raman spectroscopy*-In contrast to destructive common methods to analyze the gases, this instrument performs the analysis in a nondestructive way and also the bubble size is not limited to 100µm and above, it is useful to analyses small bubbles as well[80].On the other hand sample preparation for analysis is not more than just polishing the glass surface which will be illuminated by laser light. Since this method do not damage the glass, analyses can be repeated several times even under applied different temperatures[84].

The experimental setup and the working principle of Raman Spectroscopy are in Chapter 2.

3.2.4 Results

The samples produced in the same production line of the glass-making company were used in this study and the type of the trapped gas inside bubble defects was analyzed by using the non-destructive Raman Spectroscopy method. The shape of the bubble seeds can be seen in the figure 3.24.

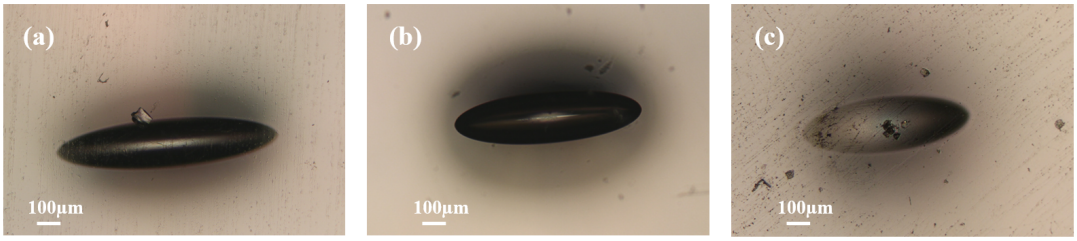

Figure 3.24: (a),(b),(c)The bubble defects on different glass samples

When zooming on the bubble defects by optical microscope, the different regions inside the bubble appeared. These regions can be divided into parts as the center and the left, and the right corner as in the figure 3.25.

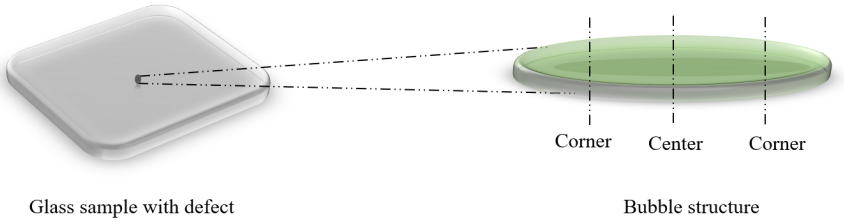

Figure 3.25: Bubble defect regions

The high-intensity laser light was focused on each region and corresponding signals were collected with a total of 2 accumulations and 100 sec integration time. Since the dept of the bubbles is different in each region, the laser focus was made carefully and the scattering effect was considered in the laser alignment on the regions (see figure 3.26).

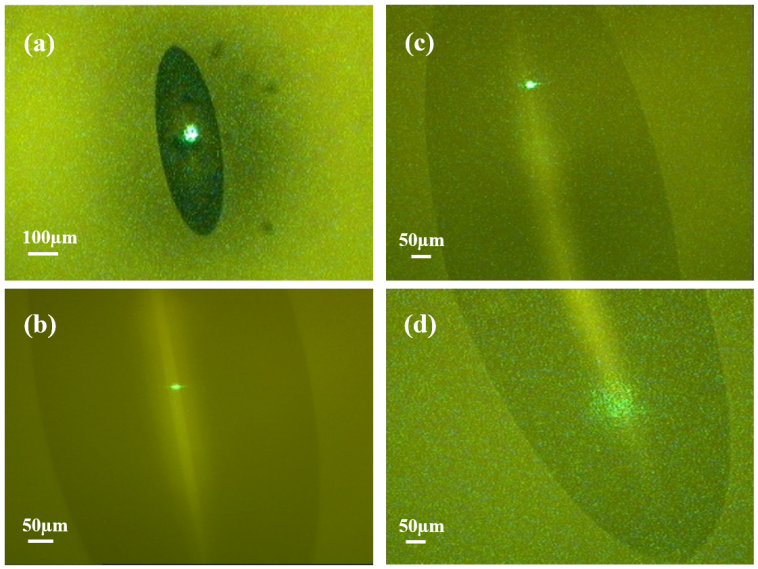

Figure 3.26: (a),(b) Laser focuses on the bubble center region;(c),(d) Laser focuses on the bubble corner region

The results (see figure 3.27) shows the presence of some aforementioned bubble forming effects contribution in the bubble trapped gas. While both center and the corner of the bubble regions had the presence of refractory materials and raw materials, only the center of bubble showed the presence of used fining agents like Senarmontite Sb_2O_3 and the sulphur which plays an important role in the melting process [88]. As a result, the interaction between glass melt and the refractories on the furnace wall and the feldspar which is used to lower the meltin temperature of the silica in the batch during the melting process could be the reason for the observing these peaks.

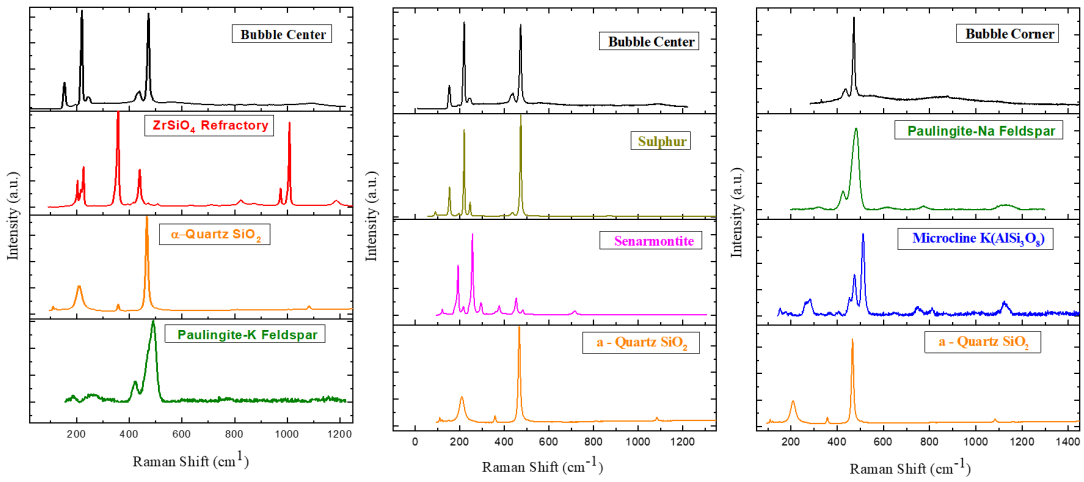

Figure 3.27: Raman Spectroscopy results for the peak analyses of the trapped gas inside the bubble defects

Chapter 4

Conclusion

In this thesis, the optical methods have been used to characterization of wide range of materials from macro sized glass samples to nano size exfoliated crystals and nanowires. It was identified the compounds of trapped gases inside a bubble defect in the glass via scattering of light which is used in operation of Raman Spectroscopy. Non-destructive Raman measuremenets were performed on different glass samples and the fingerprint information of the specific compounds were obtained in a matter seconds. In addition to diffraction-limited Raman measurements, the high-spatial frequency components of the light in near-field zone were tried to collet by operating transmission mode near-field Raman spectroscopy. The experiences and outcome of this work was reported in apendix section. The operation of transmission mode near-field microcopy provides very useful and local information in nanosize imaging, however the challenges may end the experiments therefore the sample preparation methods and the selection of probe should match with the operation mode of the near-field system. On the other hand, the photocurrent generation of silver nanowire and nanowire networks was obtained and the mechanism behind the photoresponse were explained in details. In the device fabrication process of silver nanowire study, the biggest problem while working with nanowires is the PVP encapsulation of nanowires which increases contact resistance, therefore it is detrimental to overall device

performance. By applying a proper post-treatment method based on the diameter and length of nanowires, the elimination of PVP can be performed in the next experiments. On the other hand, the change in resistance and the temperature in the measurement process may result in local oxidation of Ag NWs under ambient conditions, so this may need to be investigated as well. Since the photocurrent generation mechanism of silver nanowires is considered based on the bolometric effect by the contribution of surface plasmon polaritons propagations, there are some factors that may need to be considered. The photoresponse nature of the bolometric effect can be affected by environmental conditions such as substrate effect, atmosphere, or environment humidity [59], therefore the influence of these factors on device performance may be further investigated. Moreover, the presence and the behavior of SPPs in the nanowire network can be examined more by performing photocurrent scans with differently polarized laser light.

Bibliography

[1] J. Weiner and F. Nunes, *Light-matter interaction: physics and engineering at the nanoscale*. Oxford University Press, 2017.

[2] Vilnius University, "Light and matter."

[3] W. Zhang, Z. Fang, and X. Zhu, "Near-field raman spectroscopy with aperture tips," *Chemical reviews*, vol. 117, no. 7, pp. 5095–5109, 2017.

[4] Northeastern University, "Diffraction."

[5] V. K. Satish, "Material science," 2009.

[6] J. Coderre, "22.55 j principles of radiation interactions. fall 2004. massachusetts institute of technology: Mit opencourseware," 2004.

[7] R. Graham and D. Yu, "Scanning photocurrent microscopy in semiconductor nanostructures," *Modern Physics Letters B*, vol. 27, no. 25, p. 1330018, 2013.

[8] Y. Gu, J. Romankiewicz, J. David, J. Lensch, L. Lauhon, E.-S. Kwak, and T. Odom, "Local photocurrent mapping as a probe of contact effects and charge carrier transport in semiconductor nanowire devices," *Journal of Vacuum Science & Technology B: Microelectronics and Nanometer Structures Processing, Measurement, and Phenomena*, vol. 24, no. 4, pp. 2172–2177, 2006.

[9] J. Park, Y. Ahn, and C. Ruiz-Vargas, "Imaging of photocurrent generation and collection in single-layer graphene," *Nano letters*, vol. 9, no. 5, pp. 1742–1746, 2009.

[10] T. Kasirga, N. Mehmood, H. Rasouli, and O. Cakiroglu, "Photoresponse in metallic layered transition metal dichalcogenides," in *APS March Meeting Abstracts*, vol. 2018, pp. R37–002, 2018.

[11] M. Buscema, J. O. Island, D. J. Groenendijk, S. I. Blanter, G. A. Steele, H. S. van der Zant, and A. Castellanos-Gomez, "Photocurrent generation with two-dimensional van der waals semiconductors," *Chemical Society Reviews*, vol. 44, no. 11, pp. 3691–3718, 2015.

[12] E. Pfitzner, X. Hu, H. Schumacher, A. Hoehl, D. Venkateshvaran, M. Cubukcu, J.-W. Liao, S. Auffret, J. Heberle, J. Wunderlich, *et al.*, "Near-field magneto-caloritronic nanoscopy on ferromagnetic nanostructures," *AIP Advances*, vol. 8, no. 12, p. 125329, 2018.

[13] T. Mueller, F. Xia, M. Freitag, J. Tsang, P. Avouris, *et al.*, "Role of contacts in graphene transistors: A scanning photocurrent study," *Physical Review B*, vol. 79, no. 24, p. 245430, 2009.

[14] H. Fukuda and M. Ohtsu, "Near-field photocurrent measurements of si pn junction under the reverse-bias condition," *Japanese Journal of Applied Physics*, vol. 40, no. 3B, p. L286, 2001.

[15] J. Hsu, E. Fitzgerald, Y. Xie, and P. Silverman, "Near-field scanning optical microscopy imaging of individual threading dislocations on relaxed ge x si1-x films," *Applied physics letters*, vol. 65, no. 3, pp. 344–346, 1994.

[16] Z. Cao, M. Ermes, S. Lehnen, R. Carius, and K. Bittkau, "Effect of topography-dependent light coupling through a near-field aperture on the local photocurrent of a solar cell," *Physical Chemistry Chemical Physics*, vol. 20, no. 2, pp. 1098–1104, 2018.

[17] M. S. Leite, M. Abashin, H. J. Lezec, A. Gianfrancesco, A. A. Talin, and N. B. Zhitenev, "Nanoscale imaging of photocurrent and efficiency in cdte solar cells," *ACS nano*, vol. 8, no. 11, pp. 11883–11890, 2014.

[18] T. S. Kasirga, "Thermal conductivity measurements via the bolometric effect," in *Thermal Conductivity Measurements in Atomically Thin Materials and Devices*, pp. 29–50, Springer, 2020.

[19] E. Hecht, *Optics*. Pearson Education, 2017.

[20] C. V. Raman, "On the molecular scattering of light in water and the colour of the sea," *Proceedings of the Royal Society of London. Series A, Containing Papers of a Mathematical and Physical Character*, vol. 101, no. 708, pp. 64–80, 1922.

[21] G. Desiraju, "The raman effect," *Nature India*, pp. 1–3, 2008.

[22] J. R. Ferraro, *Introductory raman spectroscopy*. Elsevier, 2003.

[23] H. G. Edwards, "Modern raman spectroscopy?a practical approach. ewen smith and geoffrey dent. john wiley and sons ltd, chichester, 2005. pp. 210. isbn 0 471 49668 5 (cloth, hb); 0 471 49794 0 (pbk)," 2005.

[24] E. Bailo, *Nanoscale tip-enhanced Raman scattering (TERS) for biomolecular analyses*. PhD thesis, Dissertation (TU Dortmund, Dortmund, 2009), 2009.

[25] M. Affatigato, *Modern glass characterization*. John Wiley & Sons, 2015.

[26] Witech GMbh, *System Description*, 2016.

[27] SEMrock, "Edge filters vs. notch filters for raman instrumentation."

[28] B. Bhushan, H. Fuchs, and M. Tomitori, *Applied scanning probe methods V: Scanning probe microscopy techniques*. Springer Science & Business Media, 2007.

[29] Y. Kim, Y. Lee, H. Kim, S. Roy, and J. Kim, "Near-field exciton imaging of chemically treated mos 2 monolayers," *Nanoscale*, vol. 10, no. 18, pp. 8851–8858, 2018.

[30] Y. Lee, S. J. Yun, Y. Kim, M. S. Kim, G. H. Han, A. Sood, and J. Kim, "Near-field spectral mapping of individual exciton complexes of monolayer ws 2 correlated with local defects and charge population," *Nanoscale*, vol. 9, no. 6, pp. 2272–2278, 2017.

[31] O. Ergün, "Transparent thin film heaters based on silver nanowire networks," Master's thesis, MIDDLE EAST TECHNICAL UNIVERSITY, 2015.

[32] E. Ö. GÜNER, *Silver Nanowire Networks on Polydimethysiloxane for Organic and Perovskite solar cell electrodes.* PhD thesis, MIDDLE EAST TECHNICAL UNIVERSITY, 2019.

[33] S. Coskun, B. Aksoy, and H. E. Unalan, "Polyol synthesis of silver nanowires: an extensive parametric study," *Crystal Growth & Design*, vol. 11, no. 11, pp. 4963–4969, 2011.

[34] D. Tan, C. Jiang, Q. Li, S. Bi, and J. Song, "Silver nanowire networks with preparations and applications: a review," *Journal of Materials Science: Materials in Electronics*, pp. 1–28, 2020.

[35] Nanoshel, "Top grade metal nanowires/nanorodes."

[36] Ş. Coşkun, "Applications of silver nanowire networks in opto-electronic devices," 2018.

[37] M. Khademalrasool and M. Farbod, "A simple and high yield solvothermal synthesis of uniform silver nanowires with controllable diameters," *Journal of Nanostructures*, vol. 5, no. 4, pp. 415–422, 2015.

[38] H. Mao, J. Feng, X. Ma, C. Wu, and X. Zhao, "One-dimensional silver nanowires synthesized by self-seeding polyol process," *Journal of nanoparticle research*, vol. 14, no. 6, pp. 1–15, 2012.

[39] M. Kaikanov, A. Kemelbay, B. Amanzhulov, G. Demeuova, G. Akhtanova, F. Bozheyev, and A. Tikhonov, "Electrical conductivity enhancement of transparent silver nanowire films on temperature-sensitive flexible substrates using intense pulsed ion beam," *Nanotechnology*, vol. 32, no. 14, p. 145706, 2021.

[40] A. Morag and R. Jelinek, "?bottom-up? transparent electrodes," *Journal of colloid and interface science*, vol. 482, pp. 267–289, 2016.

[41] D. Langley, M. Lagrange, G. Giusti, C. Jiménez, Y. Bréchet, N. D. Nguyen, and D. Bellet, "Metallic nanowire networks: effects of thermal annealing on electrical resistance," *Nanoscale*, vol. 6, no. 22, pp. 13535–13543, 2014.

[42] C.-L. Kim, J.-Y. Lee, D.-G. Shin, J.-S. Yeo, and D.-E. Kim, "Mechanism of heat-induced fusion of silver nanowires," *Scientific reports*, vol. 10, no. 1, pp. 1–8, 2020.

[43] E. C. Garnett, W. Cai, J. J. Cha, F. Mahmood, S. T. Connor, M. G. Christoforo, Y. Cui, M. D. McGehee, and M. L. Brongersma, "Self-limited plasmonic welding of silver nanowire junctions," *Nature materials*, vol. 11, no. 3, pp. 241–249, 2012.

[44] X. Xia, B. Yang, X. Zhang, and C. Zhou, "Enhanced film conductance of silver nanowire-based flexible transparent & conductive networks by bending," *Materials Research Express*, vol. 2, no. 7, p. 075009, 2015.

[45] T. Tokuno, M. Nogi, M. Karakawa, J. Jiu, T. T. Nge, Y. Aso, and K. Suganuma, "Fabrication of silver nanowire transparent electrodes at room temperature," *Nano research*, vol. 4, no. 12, pp. 1215–1222, 2011.

[46] J. Lee, I. Lee, T.-S. Kim, and J.-Y. Lee, "Efficient welding of silver nanowire networks without post-processing," *Small*, vol. 9, no. 17, pp. 2887–2894, 2013.

[47] J. Gu, X. Wang, H. Chen, S. Yang, H. Feng, X. Ma, H. Ji, J. Wei, and M. Li, "Conductivity enhancement of silver nanowire networks via simple electrolyte solution treatment and solvent washing," *Nanotechnology*, vol. 29, no. 26, p. 265703, 2018.

[48] C.-H. Hong, S. K. Oh, T. K. Kim, Y.-J. Cha, J. S. Kwak, J.-H. Shin, B.-K. Ju, and W.-S. Cheong, "Electron beam irradiated silver nanowires for a highly transparent heater," *Scientific reports*, vol. 5, no. 1, pp. 1–8, 2015.

[49] G. Deignan and I. A. Goldthorpe, "The dependence of silver nanowire stability on network composition and processing parameters," *RSC advances*, vol. 7, no. 57, pp. 35590–35597, 2017.

[50] V. H. Dao and B. J. Mapleback, "Generation of highly porous silver nanowire networks by plasma treatment and their direct application as supercapacitor electrodes," *Nanoscale*, vol. 12, no. 22, pp. 11868–11877, 2020.

[51] M. Marus, A. Hubarevich, R. J. W. Lim, H. Huang, A. Smirnov, H. Wang, W. Fan, and X. W. Sun, "Effect of silver nanowire length in a broad range on optical and electrical properties as a transparent conductive film," *Optical Materials Express*, vol. 7, no. 3, pp. 1105–1112, 2017.

[52] D. Langley, G. Giusti, C. Mayousse, C. Celle, D. Bellet, and J.-P. Simonato, "Flexible transparent conductive materials based on silver nanowire networks: a review," *Nanotechnology*, vol. 24, no. 45, p. 452001, 2013.

[53] X. Yu, X. Yu, J. Zhang, L. Chen, Y. Long, and D. Zhang, "Optical properties of conductive silver-nanowire films with different nanowire lengths," *Nano Research*, vol. 10, no. 11, pp. 3706–3714, 2017.

[54] C. Gomes da Rocha, E. Adams, C. Chisholm, T. Newton, H. Manning, F. Niosi, M. S. Ferreira, and J. Boland, "Emergence of winner-takes-all connectivity paths in random nanowire networks," *Bulletin of the American Physical Society*, 2021.

[55] A. Diaz-Alvarez, R. Higuchi, P. Sanz-Leon, I. Marcus, Y. Shingaya, A. Z. Stieg, J. K. Gimzewski, Z. Kuncic, and T. Nakayama, "Emergent dynamics of neuromorphic nanowire networks," *Scientific reports*, vol. 9, no. 1, pp. 1–13, 2019.

[56] G.-J. Jeong, J.-H. Lee, S.-H. Han, W.-Y. Jin, J.-W. Kang, and S.-N. Lee, "Silver nanowires for transparent conductive electrode to gan-based light-emitting diodes," *Applied Physics Letters*, vol. 106, no. 3, p. 031118, 2015.

[57] S. Xie, Z. Ouyang, N. Stokes, B. Jia, and M. Gu, "Enhancing the optical transmittance by using circular silver nanowire networks," *Journal of Applied Physics*, vol. 115, no. 19, p. 193102, 2014.

[58] merriam-webstar, "Bolometer definition."

[59] S. Zhang, L. Cai, T. Wang, R. Shi, J. Miao, L. Wei, Y. Chen, N. Sepúlveda, and C. Wang, "Bolometric-effect-based wavelength-selective photodetectors using sorted single chirality carbon nanotubes," *Scientific reports*, vol. 5, no. 1, pp. 1–7, 2015.

[60] M. E. Itkis, F. Borondics, A. Yu, and R. C. Haddon, "Bolometric infrared photoresponse of suspended single-walled carbon nanotube films," *Science*, vol. 312, no. 5772, pp. 413–416, 2006.

[61] B. Ezhilmaran, A. Patra, S. Benny, M. Sreelakshmi, V. Akshay, S. V. Bhat, and C. S. Rout, "Recent developments in the photodetector applications of schottky diodes based on 2d materials," *Journal of Materials Chemistry C*, vol. 9, no. 19, pp. 6122–6150, 2021.

[62] Y. Wang, W. Yin, Q. Han, X. Yang, H. Ye, Q. Lv, and D. Yin, "Bolometric effect in a waveguide-integrated graphene photodetector," *Chinese Physics B*, vol. 25, no. 11, p. 118103, 2016.

[63] O. Çakıroğlu, N. Mehmood, M. M. Çiçek, A. Aikebaier, H. R. Rasouli, E. Durgun, and T. S. Kasırga, "Thermal conductivity measurements in nanosheets via bolometric effect," *2D Materials*, vol. 7, no. 3, p. 035003, 2020.

[64] K. W. Shah and T. Xiong, "Multifunctional metallic nanowires in advanced building applications," *Materials*, vol. 12, no. 11, p. 1731, 2019.

[65] T. Kim, S. Kang, J. Heo, S. Cho, J. W. Kim, A. Choe, B. Walker, R. Shanker, H. Ko, and J. Y. Kim, "Nanoparticle-enhanced silver-nanowire plasmonic electrodes for high-performance organic optoelectronic devices," *Advanced Materials*, vol. 30, no. 28, p. 1800659, 2018.

[66] P. Bharadwaj, A. Bouhelier, and L. Novotny, "Electrical excitation of surface plasmons," *Physical review letters*, vol. 106, no. 22, p. 226802, 2011.

[67] R. M. Dickson and L. A. Lyon, "Unidirectional plasmon propagation in metallic nanowires," *The Journal of Physical Chemistry B*, vol. 104, no. 26, pp. 6095–6098, 2000.

[68] M. W. Knight, N. K. Grady, R. Bardhan, F. Hao, P. Nordlander, and N. J. Halas, "Nanoparticle-mediated coupling of light into a nanowire," *Nano Letters*, vol. 7, no. 8, pp. 2346–2350, 2007.

[69] A. Akimov, A. Mukherjee, C. Yu, D. Chang, A. Zibrov, P. Hemmer, H. Park, and M. Lukin, "Generation of single optical plasmons in metallic nanowires coupled to quantum dots," *Nature*, vol. 450, no. 7168, pp. 402–406, 2007.

[70] Z. Fang, L. Fan, C. Lin, D. Zhang, A. J. Meixner, and X. Zhu, "Plasmonic coupling of bow tie antennas with ag nanowire," *Nano letters*, vol. 11, no. 4, pp. 1676–1680, 2011.

[71] Y. Fang, Z. Li, Y. Huang, S. Zhang, P. Nordlander, N. J. Halas, and H. Xu, "Branched silver nanowires as controllable plasmon routers," *Nano letters*, vol. 10, no. 5, pp. 1950–1954, 2010.

[72] R. Yan, P. Pausauskie, J. Huang, and P. Yang, "Direct photonic–plasmonic coupling and routing in single nanowires," *Proceedings of the National Academy of Sciences*, vol. 106, no. 50, pp. 21045–21050, 2009.

[73] M. Song, *Surface plasmon propagation in metal nanowires*. PhD thesis, Université de Bourgogne, 2012.

[74] A. K. Yadav and P. Singh, "A review of the structures of oxide glasses by raman spectroscopy," *RSC advances*, vol. 5, no. 83, pp. 67583–67609, 2015.

[75] K. J. Rao, *Structural chemistry of glasses*. Elsevier, 2002.

[76] H. Scholze and A. C. Claus, "Glass: Nature, structure, and properties," *Applied Optics*, vol. 31, no. 14, p. 2400, 1992.

[77] K. Baert, W. Meulebroeck, H. Wouters, A. Ceglia, K. Nys, H. Thienpont, and H. Terryn, "Raman spectroscopy as a rapid screening method for ancient plain window glass," *Journal of Raman Spectroscopy*, vol. 42, no. 5, pp. 1055–1061, 2011.

[78] D. W. Matson, S. K. Sharma, and J. A. Philpotts, "The structure of high-silica alkali-silicate glasses. a raman spectroscopic investigation," *Journal of non-crystalline solids*, vol. 58, no. 2-3, pp. 323–352, 1983.

[79] G. S. Henderson, "The structure of silicate melts: a glass perspective," *The Canadian Mineralogist*, vol. 43, no. 6, pp. 1921–1958, 2005.

[80] H. Bach and D. Krause, *Analysis of the composition and structure of glass and glass ceramics*. Springer Science & Business Media, 2013.

[81] S. N. Moraes, D. L. Morgado, and M. Nalin, "Application of raman spectroscopy to industrial research: Determination of impurities in glass bottles," *Vibrational Spectroscopy*, vol. 100, pp. 57–63, 2019.

[82] H. Müller, C. Strubel, and K. Bange, "Characterization and identification of local defects in glass," *Scanning*, vol. 23, no. 1, pp. 14–23, 2001.

[83] E. Muysenberg and J. Ullrich, "Bubbles and blister," in *Ceramic Engineering and Science Proceedings*, vol. 24, pp. 161–174, Wiley Online Library, 2003.

[84] R. Snow and D. Sendi, "Gaseous inclusions in float glass," in *Ceramic engineering and science proceedings*, vol. 9, pp. 296–305, Wiley Online Library, 1988.

[85] H. Mills, "Use of fining agents," in *Ceram. Eng. Sci. Proc*, vol. 7, pp. 404–09, Wiley Online Library, 1986.

[86] M. Hujova and M. Vernerova, "Influence of fining agents on glass melting: a review, part 2," *Ceramics-Silikaty*, vol. 61, pp. 1–10, 2017.

[87] S. T. Ellingham, T. J. Thompson, and M. Islam, "Scanning electron microscopy–energy-dispersive x-ray (sem/edx): a rapid diagnostic tool to aid the identification of burnt bone and contested cremains," *Journal of forensic sciences*, vol. 63, no. 2, pp. 504–510, 2018.

[88] M. Arkosiova, J. Kloužek, and L. Němec, "The role of sulfur in glass melting processes," *Ceram.-Silik*, vol. 52, pp. 155–159, 2008.

[89] B. Bhushan, H. Fuchs, and M. Tomitori, *Applied scanning probe methods VIII: Scanning probe microscopy techniques*. Springer Science & Business Media, 2007.

[90] C. G. Mora, M. Hartelt, D. Bayer, M. Aeschlimann, E. Ilin, and E. Oesterschulze, "Microsphere-based cantilevers for polarization-resolved and femtosecond snom," *Applied Physics B*, vol. 122, no. 4, pp. 1–8, 2016.

[91] B. Hecht, B. Sick, U. P. Wild, V. Deckert, R. Zenobi, O. J. Martin, and D. W. Pohl, "Scanning near-field optical microscopy with aperture probes: Fundamentals and applications," *The Journal of Chemical Physics*, vol. 112, no. 18, pp. 7761–7774, 2000.

[92] T. Mitsui, Y. Imanaka, K. Takehana, T. Takamasu, K. Nakajima, and J. Kim, "Standardization of excitation efficiency in near-field scanning optical microscopy," *Analytical Sciences*, vol. 27, no. 2, pp. 139–139, 2011.

[93] Z. Cai, B. Liu, X. Zou, and H.-M. Cheng, "Chemical vapor deposition growth and applications of two-dimensional materials and their heterostructures," *Chemical reviews*, vol. 118, no. 13, pp. 6091–6133, 2018.

[94] M. Chen, B. Zhou, F. Wang, L. Xu, K. Jiang, L. Shang, Z. Hu, and J. Chu, "Interlayer coupling and the phase transition mechanism of stacked mos 2/tas 2 heterostructures discovered using temperature dependent raman and photoluminescence spectroscopy," *RSC advances*, vol. 8, no. 39, pp. 21968–21974, 2018.

[95] F. Shao and R. Zenobi, "Tip-enhanced raman spectroscopy: principles, practice, and applications to nanospectroscopic imaging of 2d materials," *Analytical and bioanalytical chemistry*, vol. 411, no. 1, pp. 37–61, 2019.

[96] E. Betzig and J. K. Trautman, "Near-field optics: microscopy, spectroscopy, and surface modification beyond the diffraction limit," *Science*, vol. 257, no. 5067, pp. 189–195, 1992.

[97] J. Kasim, Y. Ting, Y. Y. Meng, L. J. Ping, A. See, L. L. Jong, and S. Z. Xiang, "Near-field raman imaging using optically trapped dielectric microsphere," *Optics express*, vol. 16, no. 11, pp. 7976–7984, 2008.

Appendix A

Near-field Experiences

A.1 Near-field Scanning Optical Microscopy

A.1.1 Experimental set up

In this study, the high-resolution surface images of the different samples were obtained by using the transmission mode Alpha 300S SNOM (WITEC GmbH, Ulm, Germany) in contact mode. The hollow pyramid is fabricated on a silicon cantilever and the apex of the SiO_2 tip is coated with a thin layer of a metal like Aluminum.The metal coating is necessary to prevent the leakage of light through the sides of the tip[89].The dimension of the cantilever are 700 µm in length, 150 μm in width and a 5 μm thickness. The typical dimension of the pyramid is 20 μm in base and 15 μm in the height.The aperture size of the probe is typically less than 100 nm for the visible wavelength applications. The resonance frequency of the tip is 14kHz in contact mode operation. The operation of the transmission SNOM starts with the laser alingment. A 532nm continues laser beam is focused on the back side of the aperture probe by using 20X objective lens. The observation of the cantilever and the sample can be done simultanelouy in this setup by help of an inertial drive assembled to the objective turret.An inertial drive holds both the cantilever and cantilever arm while performing surface approach.Also, the speed

and the movement of the inertial drive is controlled through software, which allow the optical axis alignment of the cantiliver. Therefore, the sample-probe distance can be controlled easily by following the beam-deflection principle.

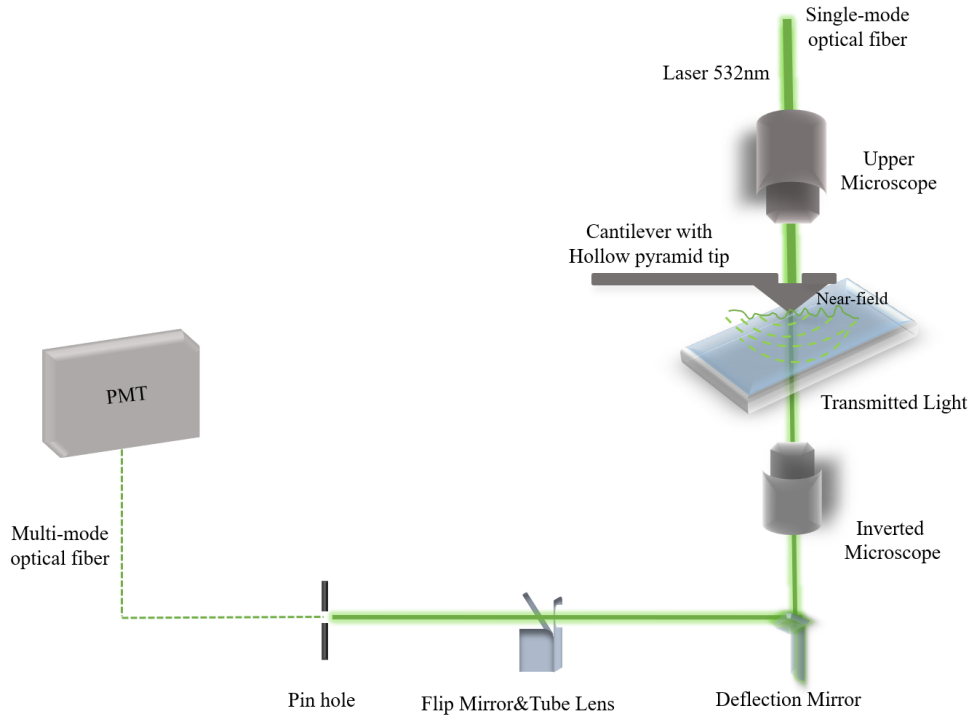

Figure A.1: Near-field Scanning Photocurrent Microscopy Setup

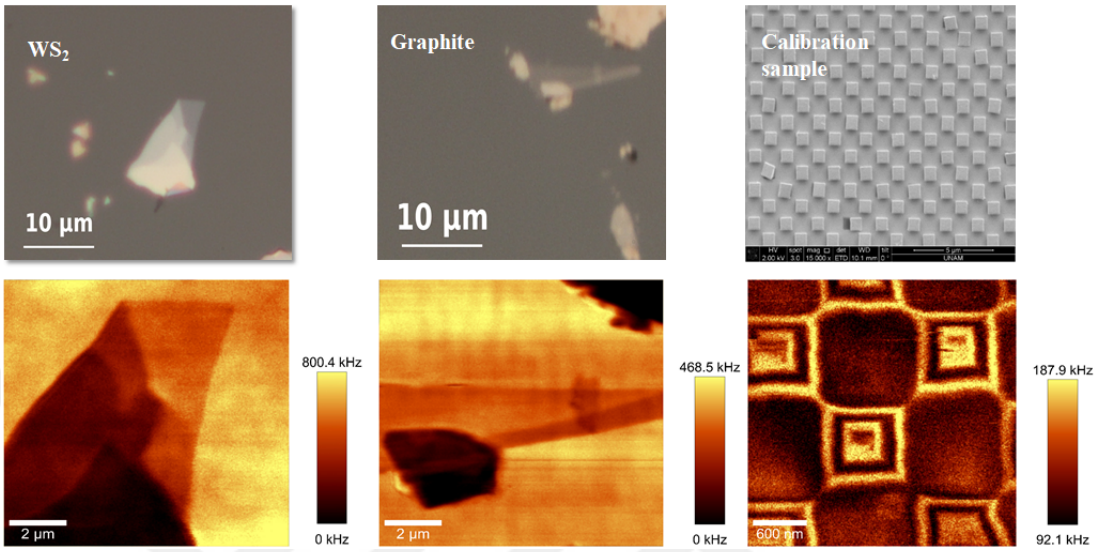

Figure A.2: Exfoliated crystals , 1x1 μm calibration sample and recorded SNOM data sets come from the feedback signals of the detector

A.1.2 Challanges

- Probe Effect

  The resolution of the image is restricted to size of the hollow pyramid probe because the transmission of the light significantly drops with decreasing aperture size [89].For instance, the drop in light transmission is in the range of 10^{-6} for an 100nm aperture size[90]. One has to always compromise from the throughput output power density to be able to obtain high-resolution. When the aperture size is smaller than 50nm, the transmission coefficient of the aperture which is defined as the power of coupled light divided by emitted light power from aperture , drops below the 10^{-4} ranges that are quite weak to be detected.[3][91].The figure 2.29 demonstrate the effect of taper angle on the transmission cofefficient of the probe [91].

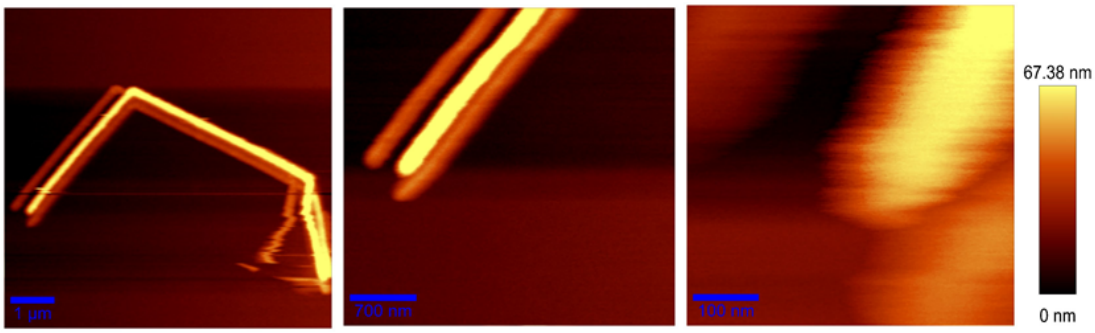

Figure A.3: Silver Nanowire SNOM topography image scan demonstrates dependency of resolution on the aperture size

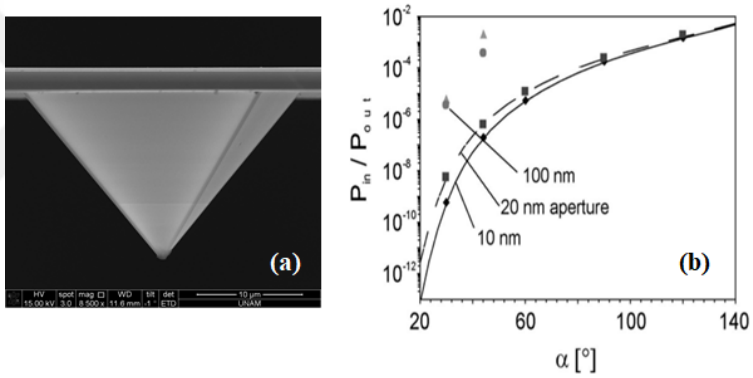

Figure A.4: (a) SEM image of the 110nm aperture size probe. The cone angle of the probe is about 65 ^{0}.(b)The transmission coefficient of different sized aperture probes as a function of the taper cone angle. Image extracted from [87]

- Device Fabrication

  The sample properties such as surface roughness, sample transparency, and the thickness of the sample can be counted as the factors on which the transmissivity of the SNOM measurement is dependent. During the surface scanning, the transmission efficiency of the near-field light changes due to the surface roughness of the sample, especially, in the usage of a blunt-ended aperture probe. As a result of the non-uniformity of the transmission efficiency, the topographic artifacts appear on the final measurement. Therefore, the sample should be prepared in such a way that the topographic changes can be eliminated as much as possible.In addition to sample thickness, the substrate effect should be taken into account in terms

of the absorption of the light. When substrate gets thinner, the absorption of the light by substrate would be minimum, thus the component of the near-field light can be detected easily by photodetector [92].

A.2 Near-field Scanning Photocurrent Microscopy

A.2.1 Experimental set up

The components of the Near-field Scanning Photocurrent microscopy can be seen in the figure A.5.The power and the intensity of the diffraction-limited 632nm laser light are controlled through the laser diode controller and laser light passes through the beam collimator before focused on the aperture probe. Once obtaining a good laser alignment on the aperture, surface approaching takes place under the control of microscope software. Once the tip gets in contact with the sample surface, the probe feeds signals from sample electrodes to lock-in amplifier through a Multifunction I/O Device to make the signal conversion from analog to digital with help of the written labview code. Such experimental parameters as scan size, step size, scan speed, and the movement of the stage are controlled through code, and in the last step, recorded signals are used to build a photocurrent map.

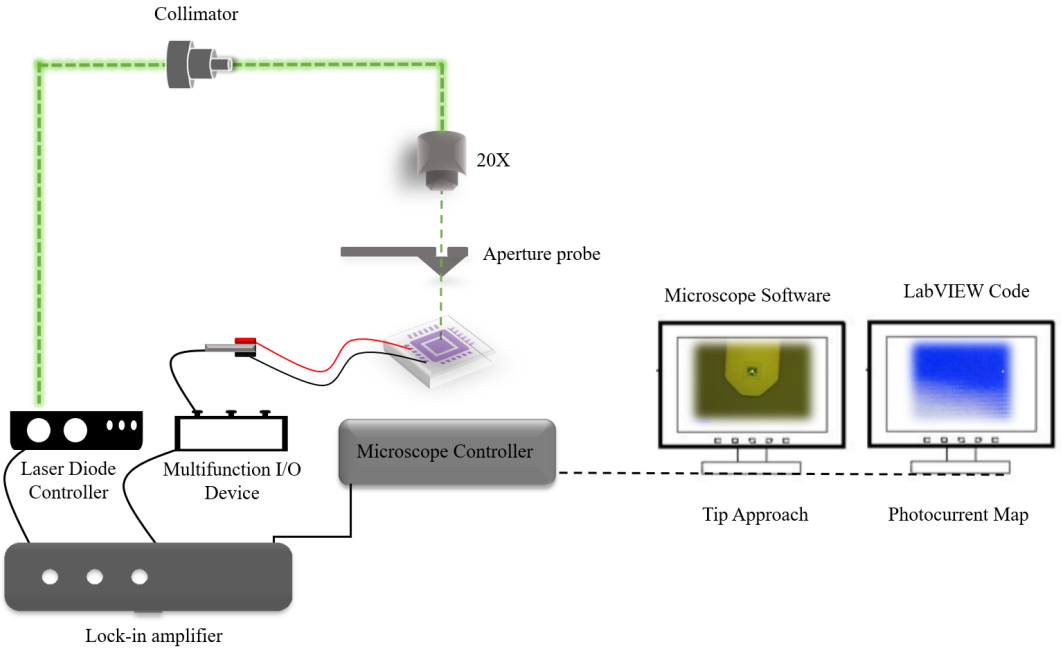

Figure A.5: Near-field Scanning Photocurrent Microscopy Setup

A.2.2 Device Fabrication

In this study, devices were fabricated in heterostructure form which is an easy way to design and prepare novel materials. The importance of building a heterostructure is because of the possibility of discovering the new properties of the material.The heterostructure form makes it possible to tune the performance of the devices by building different components to create change in the energy band alignment and the charge carried mobility of the device. Hence, the building of the designed components is very crucial to be able to create a new materials system with outstanding properties.Different 2D materials can be joined to each other by van der Waals forces, and it is not required to consider the lattice matching between different layers[93] .By upon this information, MoS_2 and TaS_2 materials were selected in this study for the purpose of designing a heterojunction form. MoS_2 is well-known for its transition in band-gap, from direct to indirect with increasing thickness of the crystal and this transition results in much yield of quantum photoluminescence. On the other hand, TaS_2 shows unique properties in the electronic and structural phases by changes in temperature [94].The device fabrication for the near-field photocurrent measurement consists of the following several steps (see figure A.6).

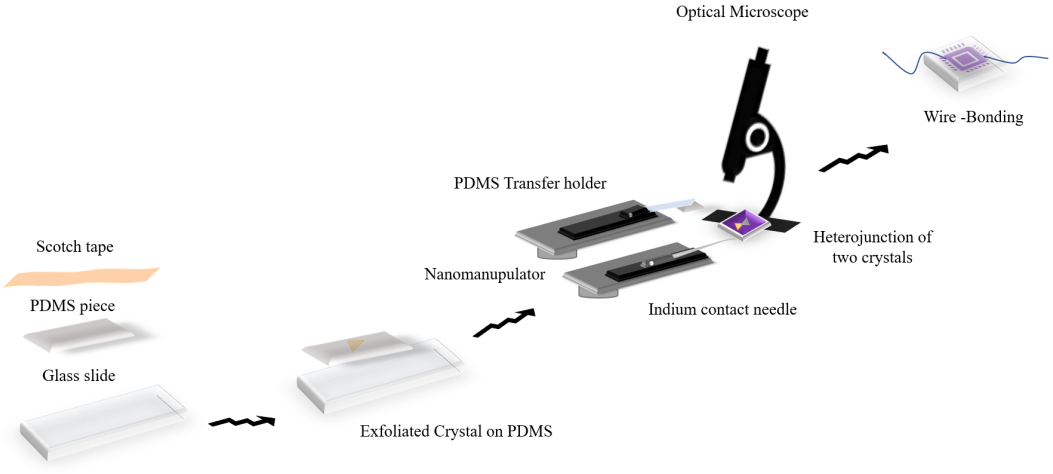

Figure A.6: Device fabrication steps for the near-field photocurrent measurement

First, scotch tape-based mechanical exfoliation of MoS_2 and TaS_2 were done on PDMS. The aim of sticking the tape on PDMS is to make crystal selection and transfer process easy and also obtain the thinnest crystal possible. Exfoliated crystals on PDMS were placed on a glass slide and fitted tightly on a nano manipulator holder. After observing under the optical microscope, the crystals were chosen for the next step which consists of an alignment of MoS_2 on TaS_2 crystal to create a junction region. By using a nano manipulator which had control in x, y, and z-direction, TaS_2 and MoS_2 crystals were carefully landed onto the surface of clean SiO_2 substrate. The final appearance of the built junction can be seen in figure A.7.

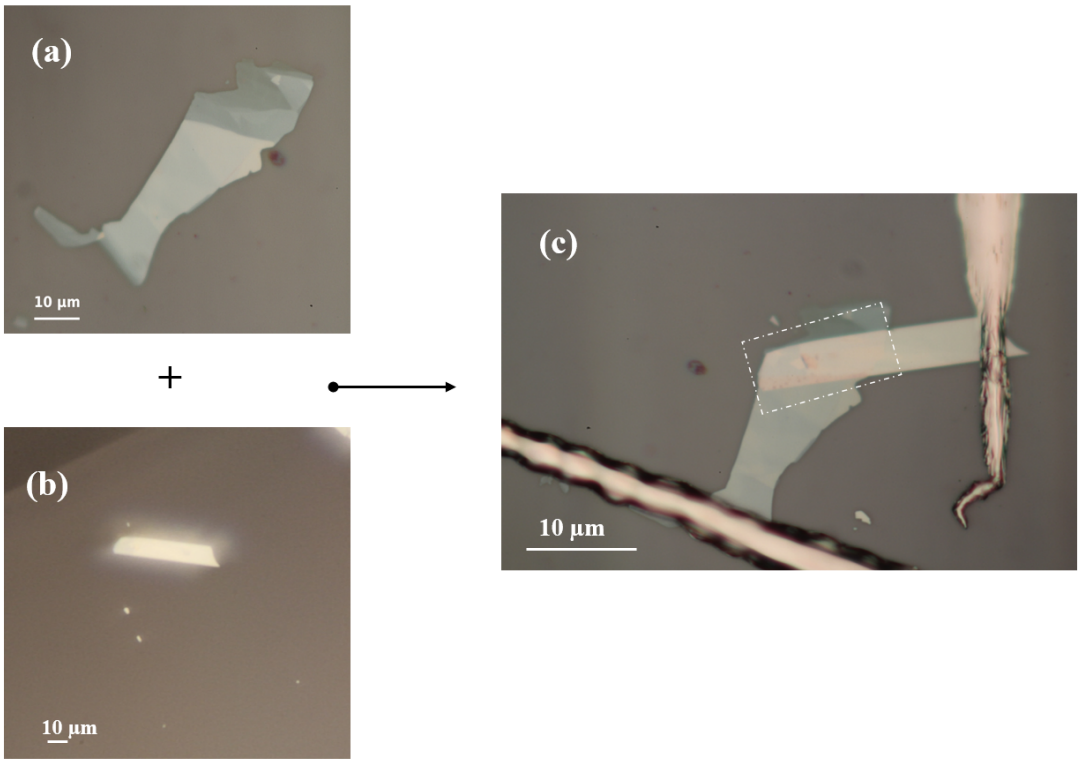

Figure A.7: (a) TaS_2 (b) MoS_2 (c) Heterojunction form

The third step was putting contacts on both sides of the junction to be able to perform electrical measurements. The indium source was melted on the copper stage and then it was dragged with the metal needle which was fitted with the holder to make a sharp indium tip. This sharp metal tip was carefully placed on the crystal. The tricky part of putting indium contact tip was to make sharp and long enough indium tails on the substrate to be able to perform a proper wire-bonding on contacts for the last step of the device fabrication process. After performing the wire-bonding with a wire-bonder in the cleanroom, the device was ready for measurement. An example of a wire-bonded device can be seen in figure A.8.

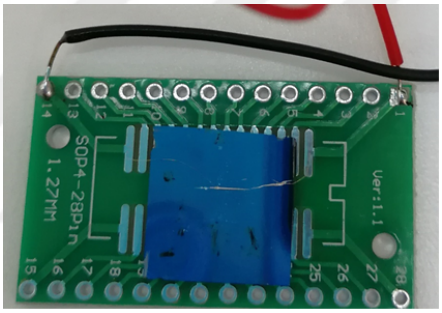

Figure A.8: Wire-bonded device

A.2.3 Challanges

The first difficulty stems from the sample preparation method. Since mechanical exfoliation is a random method with a low possibility of obtaining thin crystals, it was a less productive and time-consuming way to fabricate the device. In addition, the wire-bonded samples were easily damaged with even basic movement while placing them on the microscope stage. The second difficulty and the most severe one was the signal loss due to the aperture-based measurement system. Although the size of the aperture probe was enlarged up to 110nm, it was not enough to collect and read the meaningful signal through this configuration (see figure A.9).

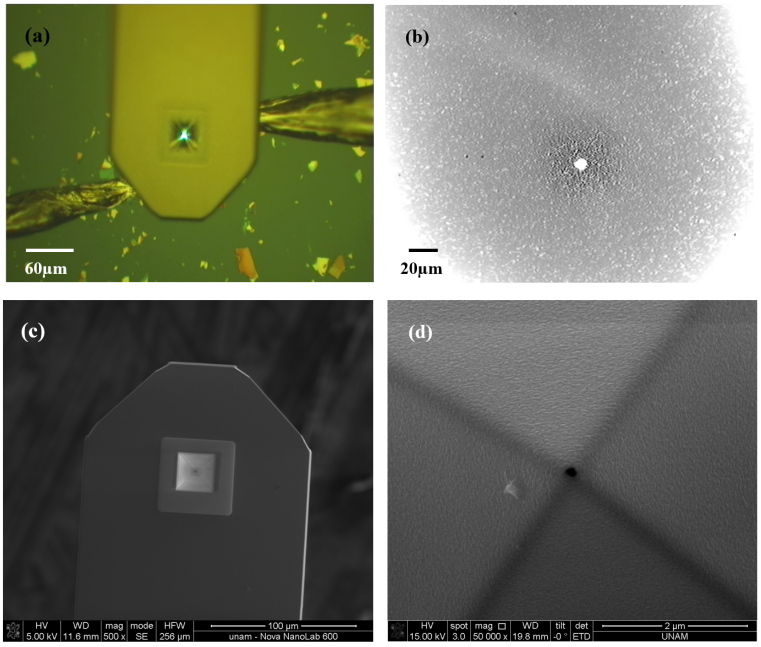

Figure A.9: (a)Upper microscope image; aperture probe is between indium contacts (b)Inverted Microscope image.Laser passing through the aperture (c)Top-view of the aperture probe (d) The apex of the aperture

A.3 Near-field Raman Specstroscopy

A.3.1 Experimental set up

Once the frequency-doubled Nd-YAG 532nm green laser light is focused through the silicon cantilever with hollow pyramid type probe(see figure A.10), an evanescent field is created at the pyramid tip of the aperture probe. With help of the piezo-driven scan stage, transmitted lights are collected spectroscopically point by point and line by line while the sample is moved and the hyperspectral imaging is obtained during the scan. The diameter of the aperture (up to 80 nm) is the only limit for the optical resolution of the transmitted light. Since AFM contact mode and beam deflection setup is used in the operation of the near-field Raman spectroscopy, the cantilever has contact with the surface of the sample. Therefore, the topographical information can also be collected at the same time along with the near-field Raman spectrum [26].

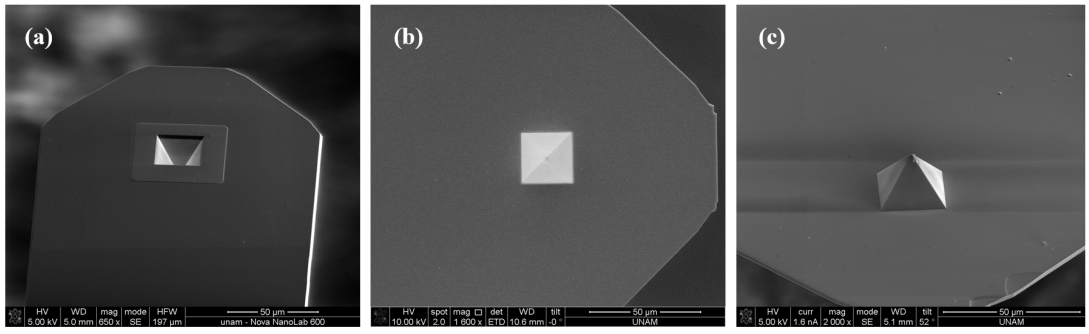

Figure A.10: (a)Top-view of the aperture probe (b) The bottom-view of the aperture (c)The hollow pyramid apex

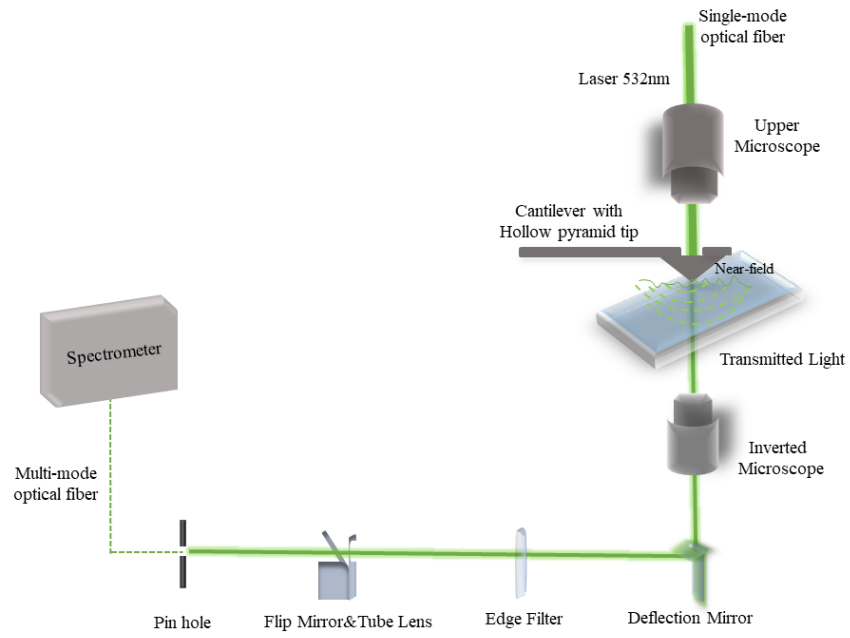

Figure A.11: Near-field Raman Setup

A.3.2 Challanges

Although having a number of advantages compared to far-field measurement methods, there are some limitations in the near-field Raman system which affect the performance of the instrument. The first limitation stems from the usage of *an aperture probe* which has been developed to overcome the diffraction limit. The probe has to have high durability, well-defined geometry, and high light transmission to be able to stand to slow and high sensitivity measurement. However, the transmission coefficient of the tip of the aperture probe significantly decrease with limiting the aperture size down to 50nm. That's also the major reason why most of the studies are carried out with the aperture size of 80 – 100nm. [3][90].Also, the amplitude of the near-field radiations exponentially decreases with increasing distance between the probe and the sample (see figure A.12) therefore the collection of the high-spatial frequency electromagnetic fields are double challenging with an aperture probe.

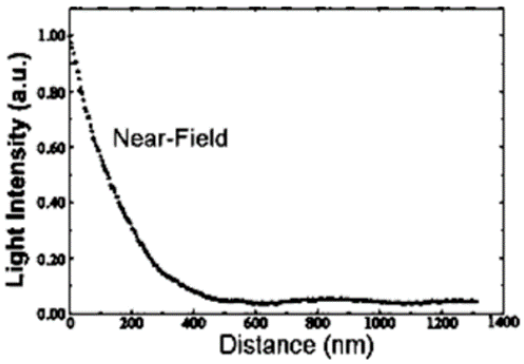

Figure A.12: The exponential decay of near-field amplitude with distance.Image extracted from [7]

In addition, the low transmission coefficient of power of the aperture probe cannot be increased by supplying more input power because of the possibility of damaging the metal coating of the probe around 10μW.Thus, one has to increase the data collection time to be able to obtain a reasonable signal-to-noise ratio because the power of the transmission coefficient around 10^{-6} for even 100nm aperture which is quite weak to be able to detect easily [3][90][91].On the other hand, it is very challenging the investigate spectroscopic information of 2D layered materials since *the material amount is extremely small*; only single molecular layer and some materials are light sensitive [95].Therefore, the sample preparation method is very critical for a correct measurement. Once created evanescent fields around the proximity of the surface, the energy shift in the transmitted light energy is collected by the inverted microscope. This is the only way to record the Raman spectrum of very small or very thin samples. When the thickness of the specimen increase, the contribution of the optically perturbative structures will be visible on the final scanned image at larger distances[96].As a result, the very long time taking of Raman mapping (e.g.$\sim$10 hours) and the limitations in specimen preparation for Transmission mode near-field Raman spectroscopy led scientists to develop an alternative approach like Tip-enhanced Raman Scattering with an apertureless probe[97].

An example result of near-field Raman mapping can be seen in the figure A.13.No meaningful near-field signals were observed after 6 hours of time-consuming measurement. Only the low-quality map of the WS_2 crystal was barely taken out. The pixel quality of the map was set in the software to the lowest value for the purpose of saving time during long measurement.

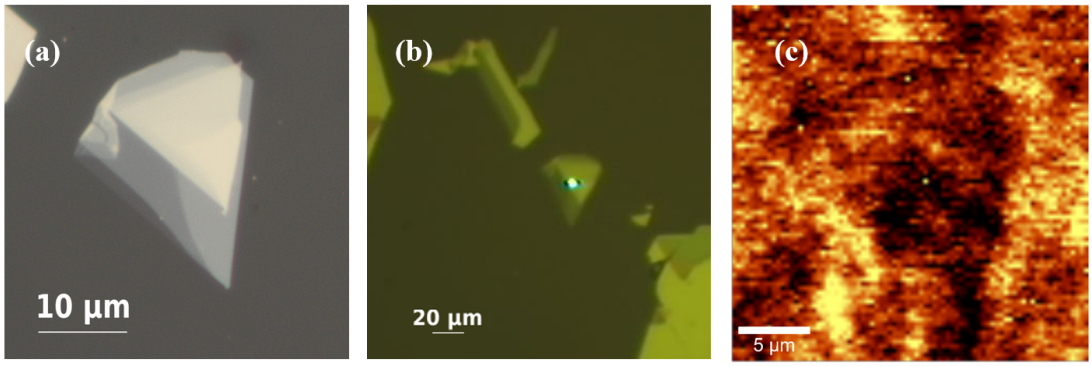

Figure A.13: (a)Optical Microscope Image of exfolaited WS_2 crystal (b)Laser light on the crystal (c) Near-field Raman mapping result